DESIGNING AND ADDITIVE MANUFACTURING OF CUSTOMIZABLE, MODULAR SCAFFOLD BLOCKS FOR LARGE BONE DEFECTS

by
Anıl Ahmet Acar

Submitted to the Graduate School of Engineering and Natural Sciences
in partial fulfillment of the requirements for the degree of
Master of Science

Sabancı University
September 2020

DESIGNING AND ADDITIVE MANUFACTURING OF CUSTOMIZABLE, MODULAR SCAFFOLD BLOCKS FOR LARGE BONE DEFECTS
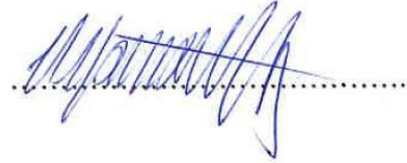
Approved by:

Prof. Dr. Bahattin Koç
(Thesis Supervisor)

Assist. Prof. Dr. Eralp Demir

Assoc. Prof. Dr. Ulaş Yaman

Approval Date: September 1, 2020

ABSTRACT

DESIGNING AND ADDITIVE MANUFACTURING OF CUSTOMIZABLE, MODULAR SCAFFOLD BLOCKS FOR LARGE BONE DEFECTS

Anıl Ahmet Acar

Master of Science in Manufcturing Engineering, September 2020

Thesis Supervisor: Prof. Dr. Bahattin Koç

Bone has an excellent capacity to regenerate itself after damage, especially for minor defects. However, for large bone defects, external intervention is needed. One of the most suitable external treatments for large bone defects is tissue engineering using a scaffold. However, the transplanted scaffold must conform to the unique morphological features of the patient's bone while providing adequate biomechanical support with the 3D porous inner structure. With additive manufacturing (AM), producing a structure that meets these requirements is possible. But the current customized scaffold design method (reverse engineering technique) is time-consuming, labor-intense and expensive due to the software and machinery used in the process (2D medical image acquisition machine, medical image processing software), and the joint work of technical and surgical staff to finalize the design of the scaffold. Depending on the complexity of the case, the design phase can take months. But in some cases, like high energy injuries, the proper treatment should be held in the fastest way possible. Otherwise, the patient may face severe and irreversible problems like unbearable pain, long hospitalized time, and even limb loss. In this thesis, a method of constructing a best fitting scaffold for the treatment of large bone defects from pre-printed modular blocks is introduced. A femur surface modeling algorithm using morphological features of the femur as input was created. With this algorithm, femur model of a patient is obtained with measuring the necessary measurements from the fewer number of 2D medical images obtained by more common methods such as x-ray images. To create modular blocks, a parametric modelling method was developed. Modules with different topological features can be created by changing the parameters in this algorithm as desired. For path planning for additively

manufacturing scaffolds, a novel algorithm has been developed where the created modular blocks are used as input and a continuous path planning is produced. As output from this algorithm, a novel, zig-zag and spiral pattern to manufacture the modules was obtained as instruction for an extrusion-based additive manufacturing process. As the last step, a system was developed that includes assembly and sequence information of the printed modules. This system informs the clinician in the field about how many of which on-demand modules they could use to create a best fitting patient specific scaffold to represent the defect area of the patient. By following the instruction, the clinician puts the proper scaffold blocks on top of each other and implants the assembled scaffold structure on the body. This study represents a promising approach in the creation of a new customized best fitting scaffold with less time, money and effort for healing large bone defects.

ÖZET

BÜYÜK KEMİK KUSURLARI İÇİN ÖZELLEŞTİRİLEBİLİR, MODÜLER DOKU İSKELE BLOKLARININ TASARIMI VE EKLEMELİ İMALATI

Anıl Ahmet Acar

Üretim Mühendisliği Yüksek Lisans Tezi, Eylül 2020

Tez Danışmanı: Prof. Dr. Bahattin Koç

Anahtar Kelimeler: Özelleştirilebilir tasarım, Eklemeli imalat, Büyük kemik kusurları

Kemik hasar sonrası özellikle küçük kusurlar için kendini yenileme konusunda mükemmel bir kapasiteye sahiptir. Fakat, büyük kemik kusurları için dış müdahaleye ihtiyaç vardır. Büyük kemik kusurları için en uygun yöntemlerden biri kemik doku iskelesi kullanarak kemik doku mühendisliğidir. Fakat, nakledilen iskele, 3B gözenekli iç yapı ile yeterli biyomekanik destek sağlarken, hastanın kemiğinin benzersiz morfolojik özelliklerine de uymalıdır. Eklemeli imalat (Eİ) ile bu gereksinimleri karşılayan bir yapı üretmek mümkündür. Ancak mevcut özelleştirilmiş doku iskele tasarım yöntemi (tersine mühendislik tekniği), süreçte kullanılan yazılım ve makinelerden (2B tıbbi görüntü alma makineleri, tıbbi görüntü işleme yazılımları) ve yapı iskele tasarımının teknik ve cerrahi personelin ortak çalışması sonucunda üretiliyor olmasından dolayı zaman alıcı, yoğun uğraş gerektiren ve pahalı olan bir yöntemdir. Vakanın karmaşıklığına bağlı olarak, tasarım aşaması aylar sürebilmektedir. Ancak bazı durumlarda, yüksek enerjili travmaya bağlı yaralanmalar gibi, uygun müdahale mümkün olan en hızlı şekilde yapılmalıdır aksi halde hasta dayanılmaz ağrı, hastanede kalma süresinde uzama ve hatta uzuv kaybı gibi ciddi ve geri dönüşü olmayan sorunlarla karşılaşabilir. Bu tezde, önceden basılmış modüler bloklardan büyük kemik kusurlarının tedavisi için en uygun doku iskelesi oluşturmak için yenilikçi bir yöntemi tanıtılmıştır. Girdiler olarak femur kemiğinin morfolojik özelliklerini kullanan bir yüzey modelleme algoritması geliştirildi. Bu algoritma ile 2B röntgen görüntüleri gibi daha yaygın yöntemlerle elde edilen daha az sayıdaki görüntülerden gerekli ölçümler yapılarak hastanın femur modeli elde edildi. Modüler bloklar oluşturmak için başka bir parametrik tasarım yöntemi geliştirildi. Bu yöntemde parametreler istenildiği gibi değiştirilerek farklı topolojik özelliklere sahip

modüller oluşturulabilir. Oluşturulan modüler blokların girdi olarak kullanıldığı ve sürekli malzeme ekstrüzyon Eİ prosesi için gerekli basım yolunun üretildiği bir algoritma geliştirilmiştir. Bu algoritmadan çıktı olarak, modülleri üretmek için yeni, zik-zak ve spiral desendeki bir basım yolu 3B yazıcıyı control etmek için geliştirildi. Son adım olarak, basılı modüller hakkında cerraha bilgi veren bir sistem geliştirildi. Bu sistem, sahadaki klinik tedavi uzmanını, hastanın kusur bölgesini en iyi şekilde temsil edecek doku iskelesini oluşturmak için hangi basılı modülden kaç tane kullanması ve sırası hakkında bilgi verir. Klinisyen bu bilgilendirmeyi takip ederek uygun doku iskele bloklarını üst üste koyar ve birleştirerek oluşturduğu bu doku iskele yapısını implant eder. Bu çalışma, özellikle büyük kemik defektleri için daha az zaman, para ve çaba harcanarak yeni, hastaya özelleştirilmiş, en uygun doku iskelenin oluşturulmasında umut verici bir yaklaşımı temsil etmektedir.

ACKNOWLEDGEMENTS

To the people who thought they are in minority and/or less fortunate.

TABLE OF CONTENTS

LIST OF TABLES

LIST OF FIGURES

LIST OF ABBREVIATIONS

CHAPTER 1 INTRODUCTION AND MOTIVATION

1.1. Introduction and Problem Statement

Bone tissue not only provides the necessary support for the body or the movement of it but also it protects internal organs and produces stem cells. That is why bone is undergoing constant remodeling, which makes the bone one of the most dynamic tissues (Kim et al. 2020). It also has a great capacity to regenerate itself in the case of an injury or a fracture. However, for large bone defects (Schemitsch 2017), resulting from high energy injuries or pathological fractures, external intervention in the form of bone substitutes is inevitable. Worldwide, bone grafting is the most common tissue transplantation after blood transfusion (Campana et al. 2014). More than 500 000 transplantation are performed each year in the US alone and this number corresponds to a quarter of the world in general (Greenwald et al. 2001). Autograft is the most common bone substitution method, but it has some limitations like prolonged operation time, donor-site morbidity, and limited resource (Keating, Simpson, and Robinson 2005). Another external intervention called allograft has also some disadvantages like immune rejection, disease transmission (Giannoudis, Dinopoulos, and Tsiridis 2005). The other external intervention is three-dimensional (3D) porous bone scaffolds.

With the recent development in tissue and manufacturing engineering, producing a bone substitute called a scaffold, that provides the necessary biomechanical properties to the bone while mimicking the tissue environment became possible. In the design of this type of substitution, the material's biocompatibility, bioresorbability, osteoconductivity, osteoinductivity, surface and failure properties should be considered (Kim et al. 2020). Because they have direct effects on biological and mechanical properties and the process of integration of bone substitute to the native tissue.

Metals, bioceramics, bioactive glasses, and polymers are the main materials used in the creation of bone scaffolds (Turnbull et al. 2018). Although metals (i.e., cobalt-chromium, zirconium, titanium, and stainless steel) have excellent biocompatibility and strength, their lack of biodegradability and possibility of releasing toxic metal ions makes them less suitable (Li et al. 2016). Bioceramics (calcium phosphate (CaP), hydroxyapatite (HA), tricalcium phosphate (TCP), biphasic calcium phosphate (BCP)) also have excellent biocompatibility. Moreover, they also have excellent osteoinductive and osteoconductive properties as well as controllable degradation. But they are hard and brittle. This feature decreases the use of bioceramics in the production of constructs that need to be load-bearing (Kim et al. 2020). Like bioceramics, bioactive glasses are also brittle. But their bioactive and osteoconductive properties are good as well. Naturally occurring polymers (collagen, silk, alginate, chitosan, hyaluronic acid) have good ductility, biocompatibility, and biodegradability properties. But the presence of pathogenic impurities (i.e., endotoxin) and not satisfying enough mechanical properties makes them less usable (Liu and Ma 2004). Synthetic polymers (poly(lactic acid) (PLA), poly(glycolic acid) (PGA), poly(caprolactone) (PCL), poly(ethylene glycol) (PEG), poly(lactic-co-glycolic acid) (PLGA)) could be used to obtain a scaffold with desired pore characteristics, degradation rate and mechanical strength. But they are generally hydrophobic, and they mostly need a surface treatment to improve bioactivity (Turnbull et al. 2018; Zhang et al. 2019).

Table 1.1 Comparison of scaffold materials (Turnbull et al. 2018).

Manufacturing Materials	Benefits	Potential Limitations
Hydrogels	• High water content/growth media inclusion allows for cell encapsulation and growth • Mechanical properties can be modified through crosslinking • Controlled drug/growth factor release possible • Ease of patterning via 3D printing to mimic tissue microarchitectures	• Mechanical properties limit use in load bearing constructs • Optimizing printing conditions for individual hydrogels can be time consuming • Physical manipulation of constructs can be difficult • Loading evenly with cells can be challenging
Polymers	• Natural polymers can be derived from extracellular matrix, ensuring high biocompatibility and low toxicity • Biodegradable • Often contain biofunctional molecules on their surface • Synthetic polymers offer improved control over physical properties	• Natural and synthetic polymers generally lack mechanical properties for load bearing • Pathological impurities such as endotoxin may be present in natural polymers • Synthetic polymers are often hydrophobic and lack cell recognition sites
Ceramics	• Osteoconductive and osteoinductive properties allow strong integration with host tissue • Similar composition to host bone mineral content	• Hard and brittle when used alone • May display inappropriate degradation/resorption rates, with decline in mechanical properties as a result

	• Can be delivered as granules, paste or in an injectable format		
Bioactive glasses	• Osteoconductive, osteoinductive properties • Adapted into clinical prosthesis already	• Inherent brittleness • Difficult to tune resorption rate • Manipulation of constructs into 3D shapes to treat specific defects challenging • Potential for release of toxic metal ions	
Metals	• Biocompatible • Superior strength • Superior mechanical properties can be advantageous in situations where slow bone growth likely	• Superior modulus can lead to stress-shielding • Poor biodegradability may result in further surgery/impairment of tissue ingrowth • Secondary release of metal ions may cause local and distal toxicity	

It is also important for scaffolds, used as bone substitutes, to have a customized external shape to allow excess removal from the defect area (Yang et al. 2019). Additionally, they should have an interconnected porous inner structure to enhance cell activity.

With several manufacturing techniques (i.e., gas foaming (Moghadam et al. 2017; Costantini et al. 2016), sol-gel (Theodorou et al. 2016; Ros-Tárraga et al. 2017), freezing drying (Abd-Khorsand, Saber-Samandari, and Saber-Samandari 2017; Fereshteh et al. 2016)), it is possible to produce porous scaffolds. However, these methods do not provide a controllable pore structure. Moreover, some of these methods leave some toxic residues which will reduce the biological properties of the bone substitutes, thus affect bone regeneration adversely. On the other hand, with additive manufacturing (AM), a relatively new manufacturing technique, it is possible to produce scaffolds not only having a customized external shape but also porous inner structure.

AM methods that could be used to produce bone substitutes can be divided into four categories. The summarized advantages and disadvantages of each category can be seen in Table 2.

Table 1.2 Rapid Prototyping (RP) techniques for bone scaffold fabrication (Bose, Vahabzadeh, and Bandyopadhyay 2013).

Technique	Process details	Processed materials for bone tissue engineering	Advantages	Disadvantages
3D Plotting/direct ink writing	• Strands of paste/viscous material (in solution form) extrusion based on the predesigned structure • Layer by layer deposition of strands at constant rate, under specific pressure • Disruption of strands according to the tear of speed	•PCL •Hydroxyapatite (HA) •Bioactive glasses •Mesoporous bioactive glass/alginate composite •Polylactic acid (PLA)/polyethylene glycol (PEG)	•Mild condition of process allows drug and biomolecules (proteins and living cells) plotting	• Heating / postprocessing needed for some materials restricts the biomolecule incorporation

		•PLA/(PEG)/G5 glass •Poly(hydroxymethylglycolide-co-ε-caprolactone) (PHMGCL) •Bioactive 6P53B glass		
Laser-assisted bioprinting (LAB)	•Coating the desired material on transparent quartz disk (ribbon) •Deposition control by laser pulse energy •Resolution control by distance between ribbon/substrate, spot size and stage movement	• HA • Zirconia • HA/MG63 osteoblast-like cell • Nano HA •Human osteoprogenitor cell • Human umbilical vein endothelial cell	•Ambient condition • Applicable for organic, inorganic materials and cells • Quantitatively controlled •3D stage movement	•Homogeneous ribbons needed
Selective laser sintering (SLS)	•Preparing the powder bed •Layer by layer addition of powder •Sintering each layer according to the CAD file, using laser source	• PCL • Nano HA • Calcium phosphate (CaP)/poly(hydroxybutyrate–co-hydroxyvalerate) (PHBV) • Carbonated hydroxyapatite (CHAp)/poly(L-lactic acid) (PLLA) • PLLA • β-Tricalcium phosphate (β-TCP) • PHBV	•No need for support •No post processing is needed	•Feature resolution depends on laser beam diameter
Stereolithography (SLA)	•Immersion of platform in a photopolymer liquid • Exposure to focused light according to desired design •Polymer solidifying at focal point, non-exposed polymer remains liquid, • Layer by layer fabrication by platform moving downward	•Poly(propylene fumarate) (PPF)/diethyl fumarate (DEF) • PPF/DEF-HA • PDLLA/HA • β-TCP	• Complex internal features can be obtained • Growth factors, proteins and cell patterning is possible	•Only applicable for photopolymers
Fused deposition modeling (FDM)	•Strands of heated polymer/ceramics extrusion through nozzle	•Tricalcium phosphate (TCP) •TCP/polypropylene (PP) • Alumina (Al_2O_3) • PCL •TCP/PCL	•No need for platform/support	•Material restriction due to need for molten phase
Robotic assisted deposition/robocasting	•Direct writing of liquid using a nozzle •Consolidation through liquid-to-gel transition	• HA/PLA • HA/PCL • 6P53B glass/PCL	•Independent 3D nozzle movement • Precise control on thickness • No need for platform/support	• Material restriction

The general steps of creating scaffold structures are: 1) acquisition of two-dimensional (2D) medical images (e.g., computed tomography (CT) or magnetic resonance imaging (MRI)) of a patient, 2) importing acquired 2D medical images into a medical image processing software, 3) reconstruction of native tissue and a 3D model representing the

fracture or bone defect area of a patient, 4) designing a virtual prototype of a customized bone substitute with the help of computer-aided design (CAD) systems, 5) producing the designed scaffold with computer-aided manufacturing (CAM) systems.
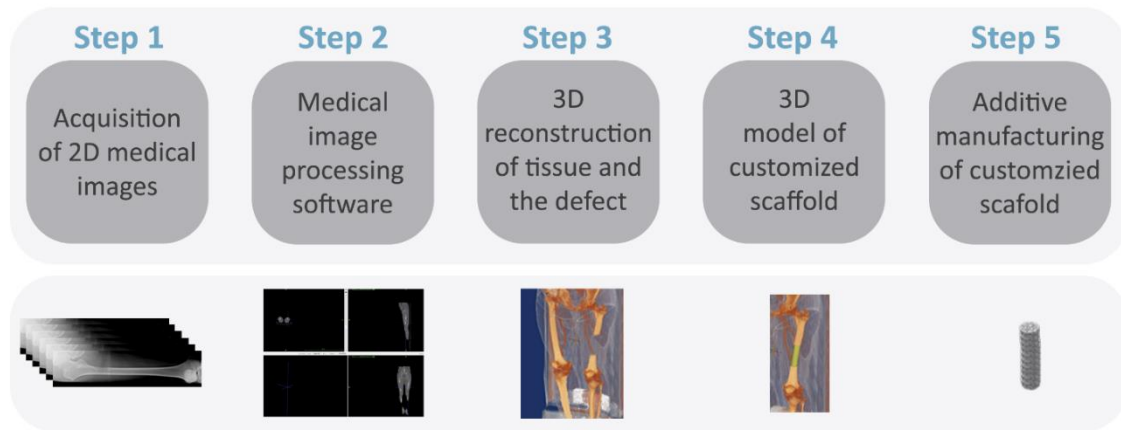
Figure 1.1 Flowchart of customized scaffold creation with additive manufacturing.

As can be understood designing and producing a scaffold structure with the explained method is time-consuming, labor-intensive, expensive, and not repeatable (Zadpoor 2020). Because, in each case, the patient and the defect size and shape changes. Moreover, when it is considered that the design of the scaffold is held with collaborative work between technical and surgical staff, depending on the complexity of the case, technical and surgical staff spend even months to finalize the design step. However, some patients such as trauma patients need proper treatment in the fastest way possible. Otherwise, they may face severe problems (McCall et al. 2010). Another drawback of the explained method is that the machinery and equipment, used in the design and manufacturing processes of a customized scaffold structure, are expensive. Furthermore, for some places such as refugee camps, underdeveloped, and/or developing countries, where a fast treatment is needed, accessing these types of machinery and equipment is limited. To avoid this, a generic scaffold could be designed and manufactured and then sent where they are needed. But since people's anthropometric measurements, thus morphological features, change with gender, age, race, etc. (Kerley 1978; Ericksen 1979; Rawal et al. 2012; Mahaisavariya et al. 2002), manufacturing a scaffold that meets the requirements of all the people seems unrealistic. That is why a surgeon in the field needs to make some modifications to the scaffold during the operation. But this procedure relies on the

surgeon's abilities and extends the operation time. It also increases the risk of complications which may result in long hospitalized time, unboreable pain and even loss limb (Rawal et al. 2012). To avoid such problems and create a best fitting scaffold to satisfy the necessary conditions, a new design paradigm regarding the creation of patient-specific modular scaffold is necessary.

1.2. Overview of Proposed Methodology

In this study, a concept of creating a customized best fitting scaffold from a range of existing "modules" is introduced as a new design paradigm. The goal is to produce enough variety in modules with rational product family architecture, so a better solution could be provided to patients needs.

Chapter 2 explains the details of the two generated algorithms and related theories. The first algorithm was generated to obtain the 3D modeling of customized modular scaffold blocks to be additively manufactured, while second one was generated to obtain a deposition path planning for continuous extrusion AM. With the second algorithm, a novel continuous tool path planning is obtained. Here, the difference in the created algorithm with the paths available in the literature was explained. After the optimization of the printing parameters, modules are additive manufactured. This chapter also gives information about printing.

Chapter 3 demonstrates the details about a generated algorithm and system. The femur surface modeling algorithm is created to model femur parametrically. By extracting the necessary inputs from 2D medical images, the necessary (i.e., the average femur model of a certain group or a femur model of a patient) model can be generated. The obtained model could be used either as a geometry-based input for the module creation algorithm, mentioned in Chapter 2, or to create the best fitting scaffold for the patient. To do that, a system is created to inform the clinician in the field about how many of which modules to use to create the best fitting scaffold and assemble them. Illustrative examples are also given in this chapter.

CHAPTER 2 BIOMANUFACTURING OF CUSTOMIZED MODULAR SCAFFOLDS FOR CRITICAL BONE DEFECTS

There is a significant unmet clinical need for modular and customized porous biodegradable constructs (scaffolds) for non-union large bone loss injuries. This chapter proposes modelling and biomanufacturing of modular and customizable porous constructs for patient-specific critical bone defects. A computational geometry-based algorithm was developed to model modular porous constructs using a parametric femur model based on the frequency of common injuries. The generated modular constructs are used to generate biomimetic path planning for three-dimensional (3D) printing of modular scaffold pieces. The developed method can be used for regenerating bone tissue for treating non-union large bone defects.

2.1. Introduction

Bone has a good healing capacity to regenerate itself for small defects. However, the regeneration potential of the bone is limited for large or critical size defects (Perry 1999). For critical bone defects, traditional methods such as internal fixation, bone shortening, External fixation and the diamond concept have been used. Internal fixation methods such as intramedullary nails or plates to stabilise bone gaps after septic conditions increase the risk of complications as recurrent infections after internal fixation and may lead to even larger defects (Scholz et al. 2015). Bone shortening with excision of the non-united bone, enables bone healing to begin immediately and assists soft tissue coverage by reducing the defect size or soft tissue tension. In cases where the defect is too large to close immediately, gradual shortening (5 mm per day) may be undertaken. However, for very large bone defects (>8 cm), shortening must be combined with other modes of treatment. External fixation based on the principle that bone and soft tissues can be regenerated under tension applied across a cortectomy, involves the application of a modular-ring external fixator with transosseous wires attached to the ring. The main advantage of this technique is that it enables early weight bearing, stimulates local blood flow, produces good quality bone and can be applied to bone defects ranging from 2 to 10 cm in size (DeCoster et al. 2004). However, it frequently presents complications caused by metal wires transfixing and cutting through soft tissues as the frame is extended to lengthen the bone (Papakostidis, Bhandari, and Giannoudis 2013).

The "diamond concept" is based on: osteogenicity (mesenchymal stem cells), osteoconduction (scaffolds), osteoinduction (growth factors), mechanical stability and vascularity. Masquelet et al. (Masquelet et al. 2000), explored the concept by proposing a two-stage method. Firstly, a cement spacer is placed in the bone defect, inducing the formation of a biological membrane around it. Secondly, the cement spacer is removed, and bone graft is placed within the tube of the induced membrane. This membrane is impermeable, hypervascular and biologically active. It forms a strong closed biological chamber after the cement removal, maintaining the volume for bone grafting, decreasing resorption of the cancellous bone and preventing ingrowth of soft tissue. Similar to this method, the use of bone grafts, particularly free vascularised bone grafts that contains an

internal vascular network, have been explored to treat bone defects allowing short union times and high union rates (Ashman and Phillips 2013). These autografts are osteogenic, osteoinductive, osteoconductive and have no risks of immunogenicity and disease transmission (Denry and Kuhn 2016). However, the main complications are related to pain and morbidity in the donor site, limited quantity and availability, prolonged hospitalization time, the need for general sedation or anaesthesia, risk of deep infection and haematoma, extended nonweight bearing and the risk of inadequate graft hypertrophy.

Recently, biofabrication, the combined use of additive manufacturing techniques, biocompatible and biodegradable materials, cells, growth factors, etc., have been explored to produce bioactive scaffolds (synthetic grafts), as an alternative to biological grafting (Bartolo et al. 2012; Pereira and Bártolo 2015). These scaffolds can be designed to match the defect site, being produced in a controlled and reproducible way using a wide range of polymers, ceramics, and polymer/ceramic mixtures. Several compositions and scaffolds with different topologies and pore sizes were produced and assessed from a mechanical and biological point (Domingos et al. 2013; Wang et al. 2016; Fiedler et al. 2015; Vorys et al. 2015; A. K. M. Khoda, Ozbolat, and Koc 2013; A. K. M. B. Khoda and Koc 2013), presenting promising results in animal studies (Caetano et al. 2016). Degradation studies and the effect of process conditions on the performance of these scaffolds has also been investigated. To achieve a uniform resorption of the scaffolds, degradation of polymer and ceramic materials must be controlled.

In summary, there is a significant unmet clinical need for a solution for the treatment of large bone loss injuries. We aim to develop a modular and customized porous biodegradable con-struct (scaffold) for non-union large bone loss injuries. In this paper we present methods for modelling and biomanufacturing of modular and customizable porous constructs for patient-specific critical bone defects. Computational geometry-based algorithms are proposed to model modular porous constructs using a parametric bone model based on the frequency of common injuries. The generated modular constructs are then used to generate biomimetic path planning for three-dimensional (3D) printing of modular scaffold pieces. The developed method can be used for regenerating bone tissue for treating non-union large bone defects.

2.2. 3D Modelling of Customized Modular Scaffold

To be able to generate modular porous blocks, the bone defect volume is represented with a set of parametric surfaces O. The modular blocks will be stacked up on an intramedullary implant (i.e., intramedullary femoral nail) as shown in Figure 2.1. The radius of this nail changes throughout the bone and defined as R_{nail}. The defect volume O is then segmented based on the similarities between the geometries, so similar sections can be combined based on the minimum allowable height and maximum errors h_{module}, $D_{allowable}$ respectively. Algorithm 2.1 was developed to take the defect area and segment it into MN number of modular blocks as shown in Figure 2.1. These modular blocks can be generated based on the anthropometric data, where wide range of sizes can be generated so it can be customized for a specific patient. In Algorithm 2.1, the object O is first sliced to generate contour curves $CO_q, q = 0, \dots, MN$. Then similar curves are clustered in a set of contours called $C_{ma}, m = 0, \dots, MN$ and $a = 0, \dots, A$ where m represents the number of clustered curves and a represents how many curves are in the mth cluster, with comparing the distance between $Pt_{CO_{qk}}$, k^{th} point on CO_q, and Pt_k, the corresponding k^{th} point on CO_j, with the tolerance $D_{allowable}$. To create the most similar and the least number of modules possible, each clustered contour set is replaced with a fit contour, which is represented with $C_i, i = 0, \dots, MN + 1$. To create the final 3D geometry of each different module, MO_q, each fit contour is extruded along the femoral shaft axis, $Pl_{SA_q} \backslash$ perp. In the transition zone between two different contours, lofting can be executed using different consecutive fit contours. At the final stage of the generating modules, M_q, the intramedullary femoral nail's volume is subtracted from the whole modules.
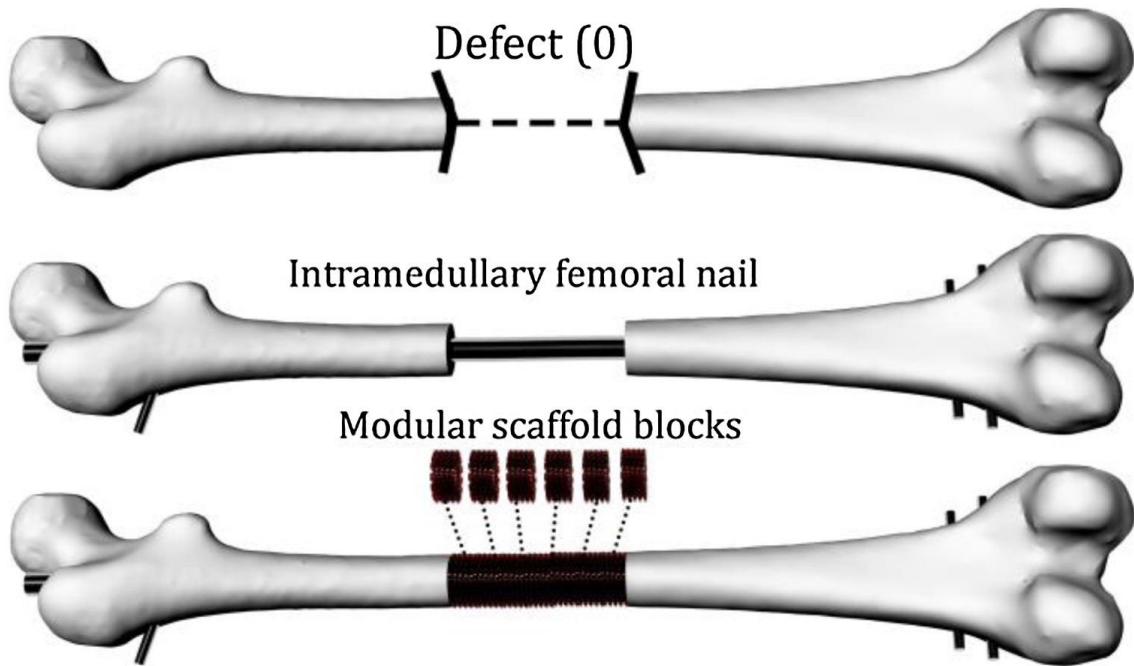
Figure 2.1 Modular scaffold blocks representing the defect volume.

After obtaining the modular blocks, they have to be porous to allow blood to bring necessary nutrition and oxygen to the defect area and also remove the waste material from it. Traditionally, the porous structures, also called tissue scaffolds, are made with regular porosity by laying opposing struts, i.e., along 0^0–90^0 angles. In this paper, the porosity is designed to change following the bone geometry. Similar to a natural bone itself, the scaffold porosity changes from the middle of the bone to outer bone biomimetically. After the scaffold modules are designed, they need to be biomanufactured using additive manufacturing (three-dimensional, 3D printing) processes. During the printing process, it is important to have a continuous path where the nozzle deposits (extrudes) biomaterial layer by layer with no- or minimum-movements between depositions. Therefore, to have biomimetically vary porosity and 3D print modular blocks continuously, a novel continuous path planning algorithm (Algorithm 2.2) is developed.

Algorithm 2.1. Creation of scaffold modules.

11

INPUT: $O, h_{module}, D_{allowable}, R_{nail}$

OUTPUT: $\{M_q\}_{q=0,...,MN}$

START

1.   **Create_Modules()** {

2. $C_q \leftarrow \{\}; CO_q \leftarrow \{\}; MO_q \leftarrow \{\}; M_q \leftarrow \{\}$ /*Initialization*/

3. $CO_q \leftarrow Intersect(O, Pl_{SA_q})$ /*The creation of representative contour curves of defect*/

4.   **While** *(i < q)* {

5. $j = i+1, m \leftarrow 0$

6.   **While** *(j < q)* {

7. $k \leftarrow 0; \alpha \leftarrow 0$

8.   **While** *(k < DN)* {

9. $P_{t_k} \leftarrow ClosestPoint(P_{t_{CO_{qk}}}, CO_j)$

10. $D = Distance(P_{t_k}, P_{t_{CO_{qk}}})$

11.   **If** *($D \leq D_{allowable}$)* {   /*Clustering the similar curves*/

12.   **If** *(k = DN−1)* {

13. $C_{ma} \leftarrow CO_i; k = k+1; j = j+1; a = a+1$

14.   **Else**

15. $k = k+1$ }   /*End of 2nd If statement*/

16.   **Else**

17. $k \leftarrow DN; j \leftarrow q$ }   /*End of 1st If statement*/

18.   }   /*End of 3rd While statement*/

19.   }   /*End of 2nd While statement*/

20. $i = i+a; m = m+1$ }   /*End of 1st While statement*/

21.   **For** *(i = 0 to m)* {

22.   **For** *(j = 0 to a)* {

23. $C_i \leftarrow FitACurve(C_{ij})$ /*The representative contours of clustered curves*/

24.   }   /*End of 2nd For-loop*/

25.   }   /*End of 1st For-loop*/

26. $CO_q \leftarrow Replace(CO_q, C_i)$ /* Replacing initial contours with fit curves*/

27.   **For** *(q = 0 to MN)* {

28. $MO_q \leftarrow Extrude(CO_q, h_{module})$

29. $M_q \leftarrow Difference(MO_q, R_{nail})$ /*Creation of the final shape of modules*/

30.   }   /*End of For-loop*/

31.   **END**   /*End of Create_Modules( )*/

END

First, the generated modular blocks sliced based on the layer thickness (nozzle diameter, D_n) and represented as cross-sectional contours. The set of cross-sectional curves are defined as $CO_n^s, n = 1, ..., B$ and $s = 1, ..., n_l$ where n_l represents the total number of layers. In the example femur case (Figure 2.2), n is given as 2.
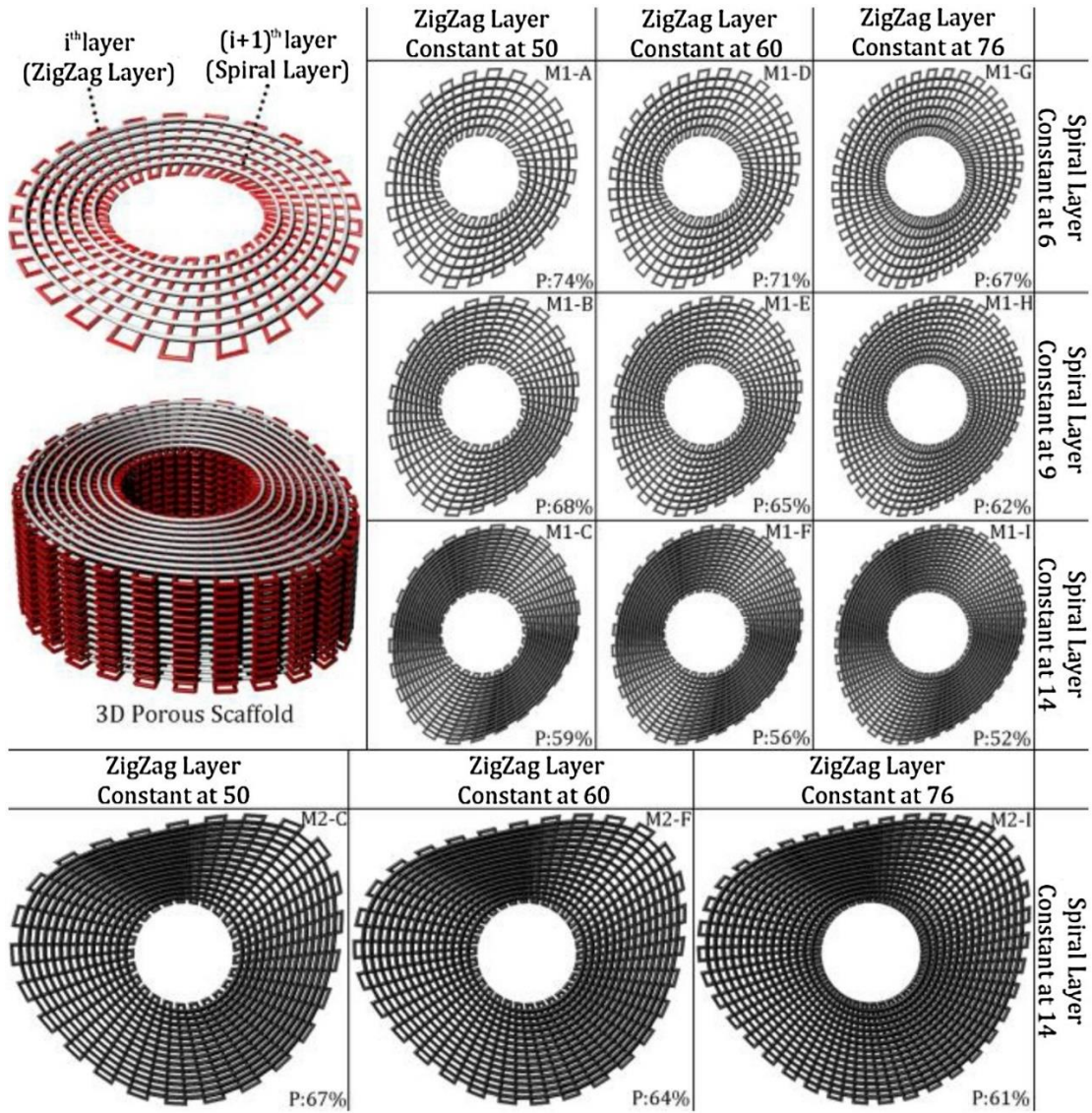
Figure 2.2 Continuous path planning and generated porous modules, (P: Porosity).

CO_0^s represents the structure's outer morphological shape at the corresponding layer *s*, and CO_1^s represents the intramedullary femoral nail's cross-sectional shape at the same layer. Algorithm 2 creates a continuous path planning using these set of cross-sectional curves. First, both curves are divided such that the distances between points are equal. These points are represented with $Pt_{CO_{ni}}^s, i = 0, \dots, DN - 1$, where *DN* represents the number of points at each contour. The points at each cross-sectional contour are matched, by minimizing the distance between them. Here, the intersection between connecting line segments and between the contours are not allowed to have any self-intersections. After the points, $Pt_{CO_{ni}}^s$, at each contour are matched, they are connected as a continuous zig-zag pattern as shown in Figure 2.2. Connecting the set of points in an orderly zig-zag

pattern (Figure 2.2), zig-zag paths are created and stored in global path planning points, $Pt_d^s, d = 0, \dots, A$, for biodegradable thermoplastic. To create the spiral pattern, lines, represented as $l_i^s, i = 0, \dots, DN - 1$, are created between each CO_n^s, and each line is divided into *DNL* number of segments to obtain the set of points called $Pt_{l_{nj}}^s, j = 0, \dots, DNL - 1$. These points are stored in global path planning points, Pt_d^s. After generating the first zig-zag pattern with *Create_ZigZag_Layers ()* function, a continuous spirallike pattern is generated at the consecutive layer with *Create_Spiral_Layers ()* function, starting from either inner or outer contour depending on where the last point of previous zig-zag pattern ends. Again, depending on where the last point of spiral pattern, at inner or outer contour, another zig-zag pattern is created for the next layer. This procedure is repeated until the whole scaffold module is generated.

By adding and connecting zig–zag and spiral patterns at each layer continuously, a 3D porous network for each modular block can be generated. Here, spiral patterns are divided into *DNL* segments. By changing the number of segments at each contour *DN* and on spiral patterns *DNL*, the desired porosity can be achieved and controlled at each layer. Figure 2.2 shows zig-zag and spiral layers with varying *DN* and *DNL* and resulting porosity levels for two different modular blocks. As shown in Figure 2.2, by changing the number of segments (*DN* or *DNL*), the porosity of the whole structure can be changed and controlled. Moreover, the porosity at each layer can be controlled by adjusting the individual parameters at each layer. This way, the porosity and micro-architecture of scaffolds can be controlled based on the mechanical and biological requirements of the targeted tissue.

Algorithm 2.2. Continuous path planning.

INPUT: $D_n, DN, DNL, \{M_q\}_{q=0,\dots,MN}$

OUTPUT: $\{P_{t_d}^s\}_{d=1,\dots,D}$

START

1. **Create_Layers()** {
2. $d \leftarrow 0; P_{t_d}^s \leftarrow \{\}$ /*Initialization*/
3.   **For** *(s = 0 to n_l)* {
4.   **If** *(s(mod 2) = 0)* **Then** {
5.   **Create_ZigZag_Layers ( )**
6.   **ElseIf** *(s(mod 2) = 1)*
7.   **Create_Spiral_Layers ( )**
8.   }   /*End of If statement*/

9.   }   /*End of For-loop*/

10. **Create_Zigzag_Layers ( )** {

11.   **For** $(i=0\ to\ 2*DN-1)$ {

12.   **If** $(i(mod\ 4)=0)$ **Then** {

13. $P^s_{t_d} \leftarrow P^s_{t_{CO_{ni}}}\ ; d=d+1$

14.   **ElseIf** $(i(mod\ 4)=1)$ **Then**

15. $P^s_{t_d} \leftarrow P^s_{t_{CO_{ni}}}\ ; d=d+1$

16.   **ElseIf** $(i(mod\ 4)=2)$ **Then**

17. $P^s_{t_d} \leftarrow P^s_{t_{CO_{ni}}}\ ; d=d+1$

18.   **ElseIf** $(i(mod\ 4)=3)$ **Then**

19. $P^s_{t_d} \leftarrow P^s_{t_{CO_{ni}}}\ ; d=d+1$ }   /*End of If statement*/

20.   }   /*End of For-loop*/

21. $s=s+1$ /*Store $P^s_{t_d}$ information for extrusion-based 3D printer*/

22. **END**   /*End of Create_Zigzag_Layers ( )*/

23. **Create_Spiral_Layers ( )** {

24. $\forall P^s_{t_{CO_{0i}}}\ and\ \forall P^s_{t_{CO_{1i}}}$

25. **For** $(i=0\ to\ DN-1)$ {

26. $l^s_i = Line\,(P^s_{t_{CO_{0i}}}, P^s_{t_{CO_{1i}}})$ /*Creation of lines that spiral paths lies on*/

27.   }   /*End of 1st For-loop*/

28. **For** $(j=0\ to\ DNL-1)$ {

29. $P^s_{t_d} \leftarrow P^s_{t_{l_{0(j-1)}}}\ ; d=d+1$

30.   **For** $(i=0\ to\ DN-1)$ {

31.   **If** $(i=DN-1)$ **Then** {

32. $P^s_{t_d} \leftarrow P^s_{t_{l_{0j}}}\ ; d=d+1$

33.   **Else**

34. $P^s_{t_d} \leftarrow P^s_{t_{l_{ij}}}\ ; d=d+1$ }   /*End of If statement*/

35.   }   /*End of 2nd For-loop*/

36.   }   /*End of 3rd For-loop*/

37. $s=s+1$ /*Store $P^s_{t_d}$ information for extrusion-based 3D printer*/

38. **END**   /*End of Create_Spiral_Layers ( )*/

END

2.3. Finite Element Analysis of Scaffolds

After the modular scaffolds are manufactured, they are stacked on the intramedullary nail

15

(implant) and allows the bone to regenerate. Here, intramedullary nail takes most of the load and keeps the modular scaffolds in their place until the bone tissue regenerates.
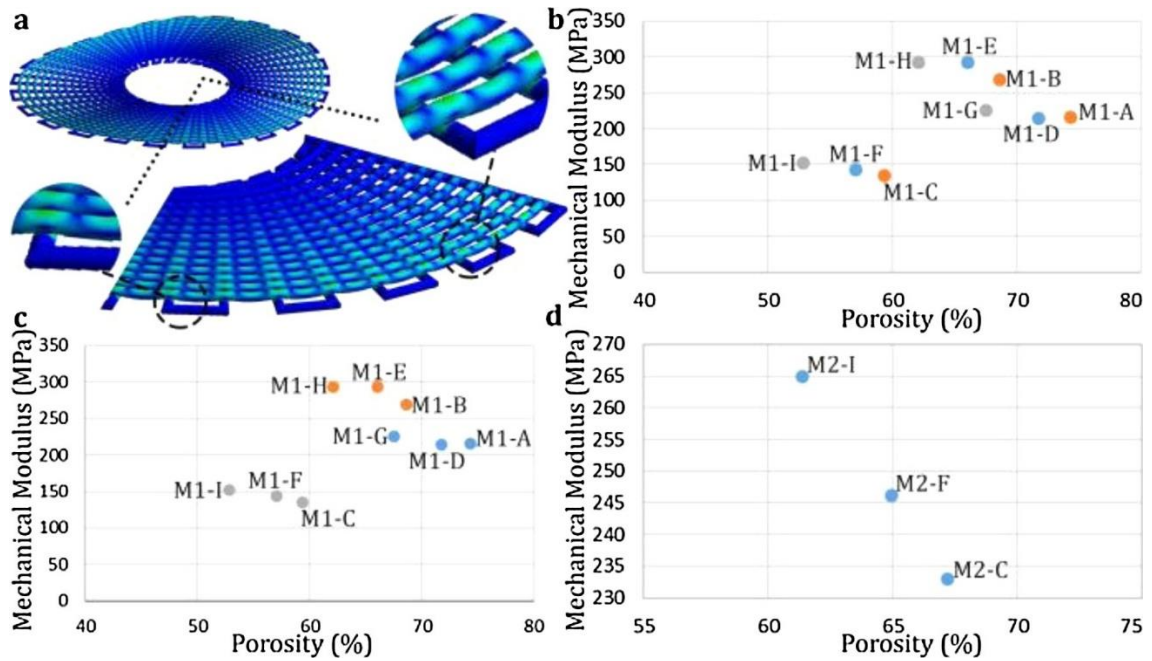
Figure 2.3 Finite-element Analysis (FEA) of generated modular scaffolds.

Although the intramedullary femoral nail is the load bearing, it is crucial for a scaffold module to provide adequate mechanical support during and after implantation. In the literature, it is stated that the mechanical modulus forhard tissue scaffolds should be in the range of 10–1500 MPa (Goulet et al. 1994). To understand the designed modular structures' mechanical modulus, a Finite Element Method (FEM) analysis of consecutive and repeated layers was performed for the different porosity levels (M1-A to -I and M2-C, F and I) as shown in Figure 2.2. As shown in (Figure 2.3a), a compression test was carried out for different porosity and different structure modules. Since the modular scaffolds will be biomanufactured using a biopolymer, Polycaprolactone (PCL), the PCL's elastic modulus $E = 300$ MPa and the Poisson ratio of 0.3 was used in the analyses (Eshraghi and Das 2010). Figure 2.3 shows the obtained result using the developed FEM. The porosity changes depending on the zig-zag pattern and spiral-pattern layer configurations. Different configurations have different mechanical modulus. Keeping the zig-zag pattern at a constant level and increasing the spiral-pattern density (Figure 2.3b) decreases the porosity level. Due to the analysis results, this increment increases the mechanical modulus, but after that, the mechanical modulus decreases. On the other hand,

keeping the spiral pattern at a constant level and increasing the zig-zag pattern also decreases the porosity level but this decreases the mechanical modulus of modular structures (Figure 2.3c). The same result is also obtained for another modular structure (Figure 2.3d). Changing the inputs of Algorithm 2.1 and 2.2 results in different structures, but they will all have an adequate mechanical modulus.

2.4. Implementation and Biomanufacturing of Modular Scaffolds for Femur Case

The developed algorithms are implemented using a Computer Aided Design (CAD) software, Rhinoceros 3D, scripting tools. For demonstration purpose, two different scaffold module design (shown in Figure 2.2) have been used. The continuous tool paths were generated and saved as an instruction to control a custom extrusion-based 3D printer. The 3D printer has a heated metal syringe where the polymeric material is loaded and attached to a head controlled in X-Y-Z-axis. By depositing heated material layer by layer in 3D, modular scaffolds blocks are manufactured. For the demonstration, the first two consecutive layers of chosen modular structures with different porosities were additively manufactured. The extrusion temperature was set at 65 ^{0}C, and a pneumatic dispensing unit was used to extrude PCL, having 37 kDa molecular weight, with 250 µm nozzle diameter. The printed final structures and their porosities can be seen in Figure 2.4a, and scanning electron microscope (SEM) images of the printed final structures can be seen in Figure 2.4b.
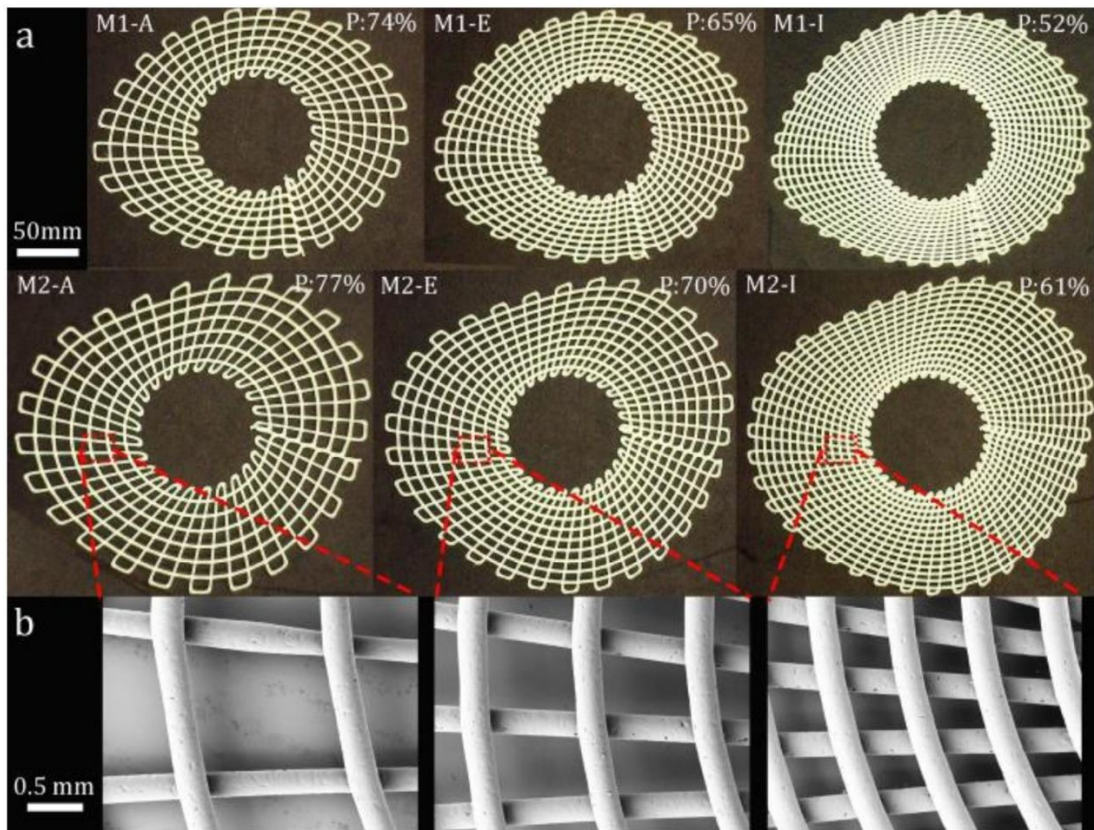
Figure 2.4 Biomanufactured modular scaffolds with varying porosity levels.

2.5. Conclusion

In this chapter, a novel method of biomimetic modeling and biomanufacturing of modular and customized scaffold blocks is presented. Computational methods were developed to generate modular blocks where they can be customized for any bone defects. The developed computational method generates a continuous deposition path plan where zig-zag pattern and spiral-like patterns followed at each layer continuously until 3D porous modules are generated. With a custom extrusion-based 3D printer, the designed porous modular blocks were additively biomanfactured with biodegradable polymers by controlling the porosity and mimicking the actual bone micro-architecture. The developed computational algorithms and the FEA model allow the user to generate modular scaffold blocks with required mechanical and biological properties. The developed methods can be used to create patient-specific scaffolds using manufactured porous scaffolds modular blocks to treat critical bone defects.

CHAPTER 3 - DESIGNING AND ADDITIVE MANUFACTURING OF CUSTOMIZABLE, MODULAR, LOW-COST SCAFFOLD BLOCKS FOR LARGE BONE DEFECTS

Additive Manufacturing (AM) has allowed to design and produce a complex three-dimensional (3D) structure, which can be patient specific, with a precise shape. With the help of advanced image acquisition techniques, image processing software, computer-aided design (CAD) and 3D printing, best fitting medical devices such as implants and scaffolds can be produced. Although implementing these techniques into the process of personalized medical device creation is helpful, some of these steps are time-consuming, labor-intense, and relatively expensive. Thus, using all these steps is not ideal when treatment is needed urgently as in trauma patients. In this chapter, a new method to create a best fitting scaffold for the shaft region of the femur of a patient from already manufactured scaffold blocks has been introduced. A femur surface modeling algorithm was created to reconstruct the femur model of a patient. This algorithm was designed around the unique morphological features of the femur. Users can extract the necessary measurements needed for algorithm from two-dimensional (2D) medical images easily. Another computational geometry-based algorithm was created to generate modular blocks. This algorithm was parametrically designed. Therefore, based on the needs of a specific group of patients, the modules with the required morphological features could be generated. Another parametric algorithm was generated to obtain a novel (zig-zag/spiral) toolpath planning for continuous extrusion additive manufacturing. With the algorithm and parameters, porous scaffold blocks with adequate biomechanical properties could be manufactured. As the final algorithm, a software restoring the information about the 3D printed modules was created. This algorithm informs the clinician about how to assemble the proper modules. The clinician puts them on top of each other with the help of an intramedullary femoral nail as instructed to create the best fitting patient specific scaffold as an external intervention for self-repairing of the large bone defect.

3.1. Introduction

Bone has a unique healing potential to regenerate itself after damage, especially for minor defects. However, for large defects which are greater than two times the diameter of the long bone diaphysis (Schemitsch 2017) external intervention is required for self-repairing. Autografts and allografts are interventions that could be held to aid bone regeneration. Nonetheless, the source of autografts is limited to fill the large bone defects or fractures. Additionally, extracting the autograft needs an additional surgical procedure which may lead to several problems (Arrington et al. 1996; Banwart, Asher, and Hassanein 1995; Flierl et al. 2013; Polo-Corrales, Latorre-Esteves, and Ramirez-Vick 2014). Although allografts could be implemented in larger quantities, accessing the resources is not always easy, especially when the treatment is urgently needed. In addition, the immune system of the patient could reject the allograft. Another external intervention for bone regeneration is scaffold.

Bone scaffolds could be manufactured with different materials. These materials must have biocompatibility, bioresorbability, osteoconductivity, osteoinductivity, and cost-effective features (e.g., metals, ceramics, and polymers) (Kim et al. 2020). Additionally, bone scaffolds should have a porous inner structure that provides a suitable environment for cells to maintain cell activity. Such scaffold structures could be manufactured with several traditional methods such as gas foaming (Ji et al. 2012), freeze-drying (X. Wu et al. 2010), fiber sintering (Pirhonen, Moimas, and Haapanen 2003), and electrospinning (Nandakumar et al. 2010). However, these methods do not provide controllable pore characteristics (e.g., pore size, pore shape, porosity), which negatively affect cellular distribution, nutrient and metabolite exchange, and thus cellular activity. This uncontrollable structure could also lead to non-uniform stress distribution inside the scaffold which leads to unpredicted mechanical properties. In addition, these methods may leave some toxic residues inside the scaffold, which will adversely affect the bone regeneration (Garg et al. 2012). On the other hand, with AM technology, bone scaffolds could be precisely manufactured with the desired interconnected porous inner structure to provide the necessary biological and mechanical properties with a proper external shape.

Designing a scaffold that can meet the requirements of all patients is unrealistic, especially considering that the morphological features of people vary with race, gender, age, etc. (Kerley 1978; Ericksen 1979; Rawal et al. 2012; Mahaisavariya et al. 2002). Moreover, in each case, the defect size and shape of a patient changes. If a scaffold does not represent the defect area accurately, a surgeon may need to make some modifications to the scaffold during the operation. This procedure, which also relies on the abilities of the surgeon, protracts the surgery time, extends the narcotizing time, and increases the possibilities of developing major complications during and after the operation which may result in long hospitalized time, unbearable pain, and even limb loss (Rawal et al. 2012). These complications can be avoided if the scaffolds are custom designed, based on the unique morphological features of patients.

With importing 2D medical imaging scans (e.g., computed tomography (CT) or magnetic resonance imaging (MRI)) into a medical image processing software, a 3D model representing the fracture or bone defect area of a patient is generated (Turnbull et al. 2018). With CAD systems, a virtual prototype of a customized bone substitute can be designed based on the obtained defect area model (Zhang et al. 2019). This design is finalized through the joint work of technical and surgical staff, to make sure that the final shape of the bone substitute meets the unique features of the individual. With computer-aided manufacturing (CAM) systems and AM, the more precise patient specific scaffold that fit the unique anatomic features of the patient and the injury is produced.

Even though AM of personalized scaffolds is very efficient, the designing and manufacturing of one such implant is time-consuming, labor-intensive, expensive, and not repeatable (Zadpoor 2020). Depending on the complexity of the case, designers and engineers spend even months to finalize the design and manufacture a customized scaffold. But, like trauma patients, some cannot wait that long, they need proper treatment in the fastest way possible. Otherwise, they may face severe and irreversible problems (McCall et al. 2010). Creating patient specific scaffolds with the mentioned method is expensive due to the machinery and equipment (e.g., clinical images, medical image processing software) needed for the design and manufacturing process. But, for some places (e.g., refugee camps, developing/underdeveloped countries) where an external intervention is urgently needed, accessing the clinical imaging or/and advanced manufacturing equipment could be limited. So, a concept of creating a customized best

fitting scaffold from a range of existing "modules" is introduced. The goal is to produce enough variety in modules with rational product family architecture, so a better solution could be provided to heterogeneous customer needs.

In this chapter, a new method to create a customized best fitting scaffold from a palette of already manufactured modules has been presented. A computational geometry-based algorithm was generated to model the femur of a patient. To manufacture the blocks with the desired properties, another parametric algorithm giving a deposition path planning for continuous extrusion AM was generated. Also, a system was developed to inform the clinician about how many of which modules should be selected from a palette of modules and how to assemble them.

3.2. Methodology

As shown in Figure 3.1, the system used to obtain the proper scaffold blocks to create a customized best fitting structure consists of two components. The first one is where an algorithm, for modeling the femur parametrically, using the morphometric measurements of people as inputs, is stored. The inputs of the algorithm in this component can be given as desired. In this way, if a dataset consists of average anthropometric measurements of a particular group (e.g., race, sex, age-group) is given, an average femur model of that group will be obtained. By using this average femur model as an input to the second component of the system, modular scaffold blocks of that specific group could be generated. If a dataset belonging to a trauma patient is given, a femur model of that patient will be obtained. The same patient specific femur model will be used to depict the defect area of the patient. In the second component, the modular blocks designed for the group that the patient belongs to are generated and stored. With the two components, a clinician in the field is informed about how many of which module to use to match the bone defect of a patient. With this assembly guidance, the surgeon selects the proper scaffold blocks from a palette of scaffold modules, containing the already printed porous biodegradable structures for that group. By placing these blocks on top of each other as instructed by the system, a best fitting scaffold for that patient could be created.
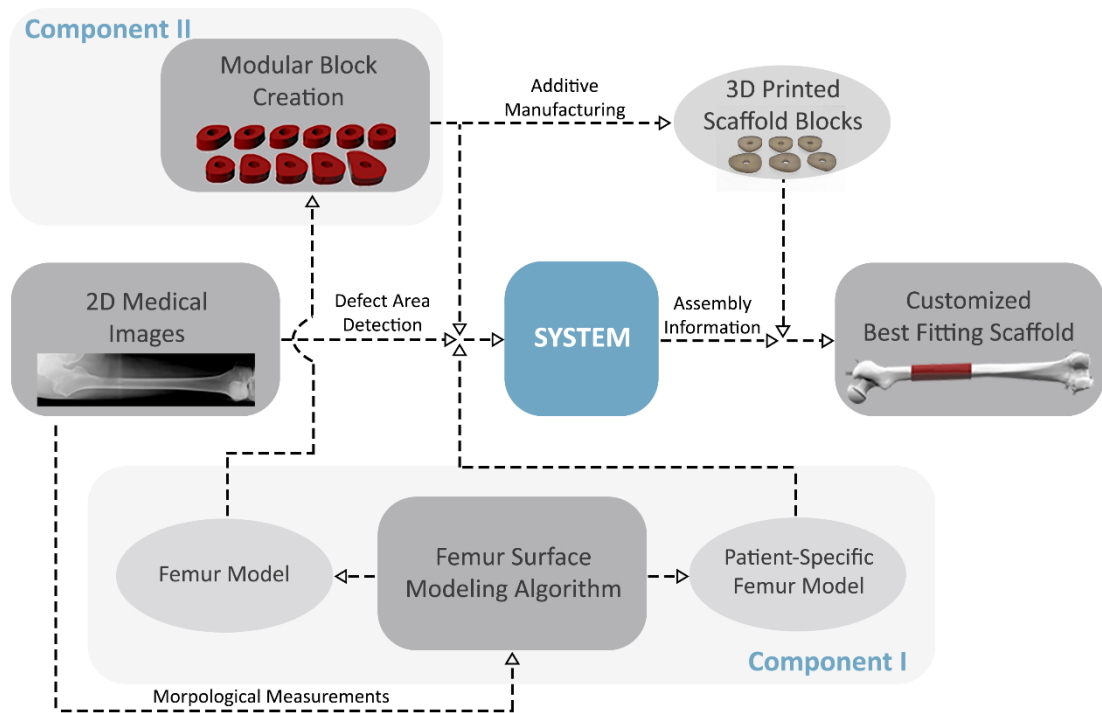
Figure 3.1 Schematic diagram of the general workflow of the created system.

3.3. 3D Parametric Modeling of Femur

The femoral surface has complex and unique morphological surface features. So, the parameterization of it is essential to create the best fitting scaffold with modular blocks. The parameterization of the femur model was satisfied with the definition of referential geometrical entities (RGEs). They not only represent the unique morphological surface features of the femur but also have significant importance for orthopedics and traumatology specialists. These entities, given in Table 3.1, are characteristic points, views, and planes and directions created with these points (Figure 3.2(a)) (Stojkovic et al. 2012; Chen et al. 2015). Like planes and directions, every element used to remodel the femur geometry (i.e., anatomic and mechanical axis) was referred to defined RGEs as well.
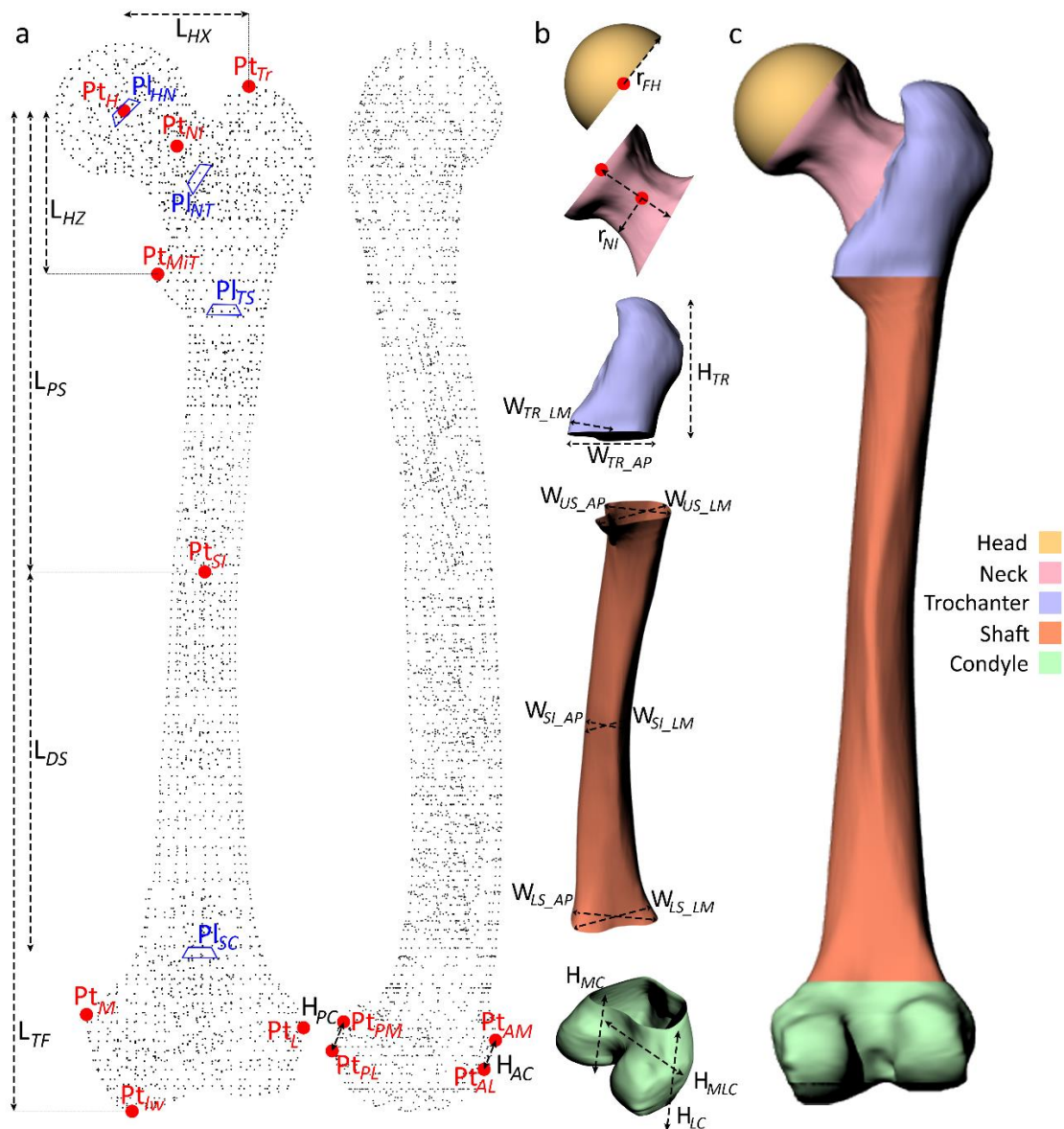
Figure 3.2 Definition of RGEs (a), FPs and MPs (a), (b) and femur regions (c).

Table 3.1 The definition of Referential Geometry Entities (RGEs).

RGE	Definition
Pt_H	Femoral head center
Pt_{NI}	Femoral neck isthmus
Pt_{Tr}	The highest point of major trochanter
Pt_{MiT}	The most prominent point of minor trochanter on medial side
Pt_{SI}	Femoral shaft isthmus – Origin
Pt_M	The most prominent point of condyle on medial side
Pt_L	The most prominent point of condyle on lateral side
Pt_{lw}	The lowest point of femur
Pt_{AM}	The most prominent point of condyle on AM

Pt$_{PM}$	The most prominent point of condyle on PM	
Pt$_{PL}$	The most prominent point of condyle on PL	
Pt$_{AL}$	The most prominent point of condyle on AL	
Pl$_{HN}$	Interface plane between head and neck	
Pl$_{NT}$	Interface plane between neck and trochanter	
Pl$_{TS}$	Interface plane between trochanter and shaft	
Pl$_{SC}$	Interface plane between shaft and condyle	

To acquire the external surface of a femur, a reverse engineering technique was performed. The obtained femur model was imported into the Grasshopper ("Grasshopper" 2020) plug-in of Rhinoceros 3D ("Rhinoceros 3D" 2020). In this plug-in, the specified RGEs were extracted on the femur model. Using the designated RGEs, the anatomical coordinate system of the femur was constructed based on the International Society of Biomechanics (ISB) suggestions (G. Wu et al. 2005). While the coordinate system was constructed, certain conditions were met, like the anatomical axis of the femur was vertical and the epicondylar axis was parallel to the coronal plane (Chantarapanich et al. 2017). It was also assumed that this would be the case for the femur models to be created in the future as well. Another use of the defined RGEs was when the femur model was divided into 5 regions, so local changes in these regions on the femur model could be made to create the new femur model of a patient or a specific group. These regions are head, neck, trochanter (greater and lesser), shaft, and condyle (Figure 3.2(c)). Using the RGEs, the necessary auxiliary planes were defined between these regions, and boundary curves between neighbouring regions (e.g., head and neck, shaft and condyle, etc.) were created. Within these boundary curves, with the help of the generated computational algorithm, the femur model was sliced with multi-planes and cross-sectional curves of those five regions were created. For these curves to be compatible with the femur to be generated, a new set of proper and necessary feature parameters, Table 3.2, was introduced in every defined femoral region. The defined femoral feature morphologies (e.g., femoral head diameter, neck and shaft length, shaft isthmus position, etc.) have direct effects on femoral biomechanical functions (Mahaisavariya et al. 2002). Moreover, with 2D medical images (e.g., x-rays of femur taken at coronal and sagittal planes), these measurements are easily accessible (Figure 3.2(a), (b)). The defined feature parameters are sufficient enough to make local morphological changes on the femur model within those regions. But they are not enough to make necessary arrangements in the femur model as a whole. To achieve this, a new set of parameters called model parameters (e.g.,

femur length, head height, total femur length, etc.) were defined, Table 2 (Chen et al. 2015). Like feature parameters, model parameters are also convenient to extract from 2D medical images (Figure 3.2(a), (b)).

In this research, the focus area for creating a customized scaffold is the shaft region, where it starts at 20 mm below from the minor trochanter, Pt_{MiT}, and ends at 20 mm above from where the condyle part begins, Pl_{SC}. FPs, and especially MPs were selected such that the representation of the shaft region would be as accurate as possible. Thus, the created customized scaffold will be the best fitting one.

Table 3.2 The definition of Feature Parameters (FPs) and Model Parameters (MPs).

FPs and MPs	Definition
r_{FH}	Femoral head radius
L_{HX}	Head offset along X-axis
L_{HZ}	Head offset from PtMiT along Z-axis
r_{NI}	Neck isthmus radius
L_N	Neck length
α_N	Neck angle
H_{TR}	Trochanter height
W_{TR_AP}	Trochanter width on AP
W_{TR_LM}	Trochanter width on LM
W_{US_AP}	Upper shaft width on AP
W_{US_LM}	Upper shaft width on LM
W_{SI_AP}	Shaft isthmus width on AP
W_{SI_LM}	Shaft isthmus width on LM
W_{LS_AP}	Lower shaft width on AP
W_{LS_LM}	Lower shaft width on LM
L_{PS}	Proximal shaft length
L_{DS}	Distal shaft length
L_{TF}	Total length of femur
α_B	Bow angle in L-M plane
H_{LC}	Lateral condylar height
H_{MC}	Medial condylar height
L_{MLC}	Medial-lateral condylar length
L_{AC}	Anterior condylar Length
L_{PC}	Posterior condylar Length

By taking both feature and model parameters as inputs for a new femur model, the anatomical and referential coordinate systems of the new femur model were constructed.

By using these inputs, the cross-sections, obtained from the initial femur model, were parametrically modelled accordingly. Using the newly constructed coordinate systems, the proportionated cross-sections were placed to proper spots with necessary transformation matrices. With lofting and filling, the freeform surface of the new femur was constructed.

3.4. Creation of "BoneBricks"

To create the modular blocks, a computational geometry-based algorithm, Algorithm 2.1, was created (Koc et al. 2019). This algorithm takes a femur model as a geometry-based input. This model could be a femur model which is thought it represents a particular group, or it could be the femur model of a patient. Additionally, this femur model could be created with the femur surface modelling algorithm as well as a reverse engineering technique. After the femur model was given as an input to Algorithm 2.1, the modular blocks of that specific group could be created with it.

This algorithm also takes some mathematical inputs like; the desired height of the module, the allowable dimensional differences between the modules, and femoral nail diameter which will be used to stack up the modules on during implantation. Based on these parameters, the shaft region of the input femur model was sliced, and cross-sectional curves of it were created based on the desired module height. With given inputs, to create the most similar and the least number of modules possible, the similar cross-sectional curves were clustered. To represent the curves in a cluster with the same contour, a fit curve was created for each group. Lofting, extrusion and some Boolean operations are performed on the fit curve sets, and the final shape of the modules were created.

3.5. AM of "BoneBricks"

A toolpath planning for continuous extrusion AM was generated with the created algorithm, Algorithm 2.2 (Koc et al. 2019). With this algorithm, it is possible to obtain

an inner porous structure with the desired mechanical and biological properties, without any blockage inside.

Algorithm 2.2 takes several mathematical parameters as inputs: Nozzle diameter, overlapping rate between layers, the desired number of divisions in two consecutive layers. It also takes the geometrical inputs which are the 3D models of the modules to be printed. In odd-numbered layers, a zig-zag like pattern was created. To create this pattern, cross-sectional curves of the module at that height was created based on the nozzle diameter, and the penetration rate. Contours were divided into equal pieces regarding the first division number input. The obtained points were stored in a matrix such that an extrusion based 3D printer will move like a zig-zag pattern at that layer. At the following layer, in even-numbered layers, the strips of the previously created zig-zag pattern, the ones will be extruded from the center to the outer, were divided with equal distances with the second division number input. The coordinate information of the obtained points was stored in another matrix based on their radial distances from the center of the intramedullary nail. While the patterns were being generated, self-intersections between the connecting line segments and contours were not permitted. Generating these patterns in two consecutive layers was repeated until the whole scaffold module was generated. The obtained matrices in each layer were merged into one global matrix. The global matrix was used to generate instructions, representing the path for the custom extrusion printer to follow, as an output of this algorithm.

3.6. Customized Scaffold Structure

An algorithm, Algorithm 3.1, has been generated to inform a clinician in the field about how a customized best fitting scaffold could be created using the already printed bone bricks, M_k, where k represents the total number of different modules. By using the same 2D medical images to obtain the femur model of a patient, $V_{patient}$, a bone defect area could be introduced to the algorithm. The two information, D_{z1}, D_{z2}, the algorithm needs to detect the defect area are the linear distances of the most prominent points of the defect along World-Z-Axis from Pt_{MiT}. With using this information, and the height of the printed modules, h_{module}, the algorithm calculates the final top and bottom planes of the

defect, Pl_t, Pl_b. These planes will be used by the surgeon to perform cutting operations on the native bone tissue to prepare it for implantation. These planes were also used to create cross-sectional curves in the defect area of the patient, $CO_q, q = 0, ..., Q$, where q represents the total number of cross-sectional curves along the defect area. Each obtained curve was divided such that the distances between the created points were equal. These points were represented with $Pt_{CO_{DN}^q}, DN = 0, ..., DN$, where DN represents the total number of points at each curve. To match the defect area with the created blocks, the obtained cross sections were compared to those of the modules, C_k. The curves that were in the allowable range, $D_{allowable}$, were moved to the right places with using appropriate transformation matrices. Thus, the customized best fitting scaffold was created. From this step, the algorithm also extracts and generates information about how to assemble, which modules are going to be used, and in what order. This instructional output, B_q, helps the surgeon to create the scaffold structure by stacking the specified modules with the help of the intramedullary femoral nail and implant the final structure to the body.

Algorithm 3.1. Creation of A Customized Scaffold with Bone Bricks.

INPUT: $V_{patient}$, D_{z1}, D_{z2}, $D_{allowable}$, M_k
OUTPUT: B, Pl_t, Pl_b
START
1. **Create_Patient_Specific_Scaffold() {**
2. $CO_q \leftarrow \{\}$; $B_q \leftarrow \{\}$ /*Initialization*/
3. Pl_t & $Pl_b \leftarrow Calculate$ $(D_{Z1}, D_{Z2}, h_{module})$ /*Calculation of the defect area that will be represented with modules*/
4. $CO_q \leftarrow CrossSection(V_{defect}, Pl_t, Pl_b, h_{module})$ /*Cross sections of the bone defect area of the patient*/
5. **While** ($i < q$) {
6. $j \leftarrow 0$
7. **While** ($j < k$) {
8. $m \leftarrow 0$
9. **While** ($m < DN$) {
10. $P_{t_i} \leftarrow ClosestPoint(P_{t_{CO_m^i}}, C_j)$
11. $D = Distance$ $(P_{t_i}, P_{t_{CO_m^i}})$
12. **If** $(D \leq D_{allowable})$ {
13. **If** ($m = DN - 1$) {
14. $V_i \leftarrow VectorCreate$ $(Pt_{Center_{C_i}}, Pt_{Center_{CO_j}})$ /*Moving the proper module to the right place*/
15. $B_i \leftarrow CopyObject(M_j, V_i)$ /*Replacing the defect area with proper modules*/
16. $m = DN$; $j = k$
17. **Else**
18. $m = m + 1$ } /*End of If Statement*/
19. **Else**
20. **If** ($j = k - 1$) {
21. $j = k$

```
22.        Else
23.            m = DN      } /*End of If Statement*/
24.                        }                    /*End of If Statement */
25.                    }                /*End of 3rd While Statement*/
26.                }                /*End of 2nd While Statement*/
27. i = i + 1
28.                }                /*End of 1st While Statement*/
29. } END                    /*End of Create_Patient_Specific_Scaffold*/
```

END

3.7. Results and Discussion

CT scans of four different femur models, Femur model A-D, were imported into Mimics version 14.1 (Materialise, Leuven, Belgium) for editing, and 3D reconstruction of them. The same femur models were also created with the generated femur surface modeling algorithm by extracting the necessary measurements from 2D medical images (Figure 3.3). To demonstrate the accuracy of the generated model by the developed algorithm, the absolute average maximum distance of the models, created with both methods, were calculated. In this study, since best fitting scaffolds are produced for the shaft region, the representation of the femur surface in that region as closely as possible to the original one is crucial. The average distance in this region of four different femur models is calculated as 1.2485 ± 0.2915 mm. Considering that the best fitting scaffolds are produced quickly, this obtained average distance in this region is acceptable (Chen et al. 2016; Noble et al. 1988).

As can be seen from Figure 3.3, femur models A, B, and C are exhibiting similar morphological features. The morphological features of the femur B represent the average femur model of these three femur models (A-C). Thus, in this study, femur model B was used as a geometry-based input during the module creation process.

As it was described earlier, besides geometry-based input, the module creation algorithm also needs some mathematical inputs like the height of the module and the tolerance. To illustrate the effect of these mathematical inputs on the modules and the representation of the femur, different palettes of modules, Table 3.3, were created for the whole defined

shaft region of Femur B (Figure 3.4). To represent the whole shaft region with modules and not to end up with some leftover areas thgrough the whole region, the defined area was divided based on the desired total number of modules that represent the whole shaft region. As a result of this number, the module height was obtained.
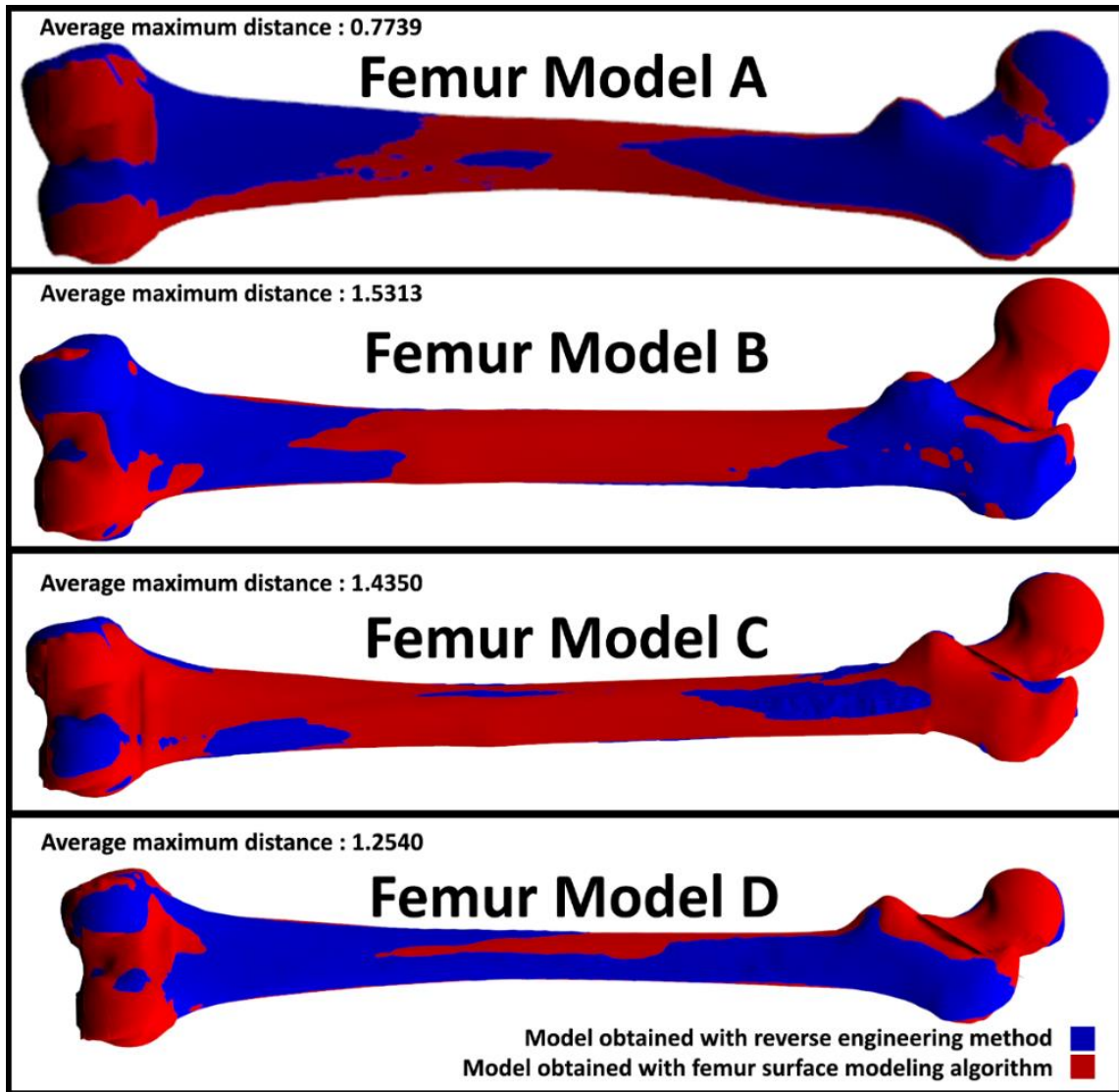
Figure 3.3 Different femur models obtained with reverse engineering method (blue ones) and the femur surface modeling algorithm (red ones).

Table 3.3 The effects of mathematical inputs on the module creation algorithm.

	Tolerance (mm)	Module Height (mm)	Total Number of Different Modules
Palette 1	0.50	5.20	25
Palette 2	1.00	5.20	14
Palette 3	2.00	5.20	7

Palette 4	0.50	10.02	19
Palette 5	1.00	10.02	12
Palette 6	2.00	10.02	7
Palette 7	0.50	15.63	15
Palette 8	1.00	15.63	10
Palette 9	2.00	15.63	5
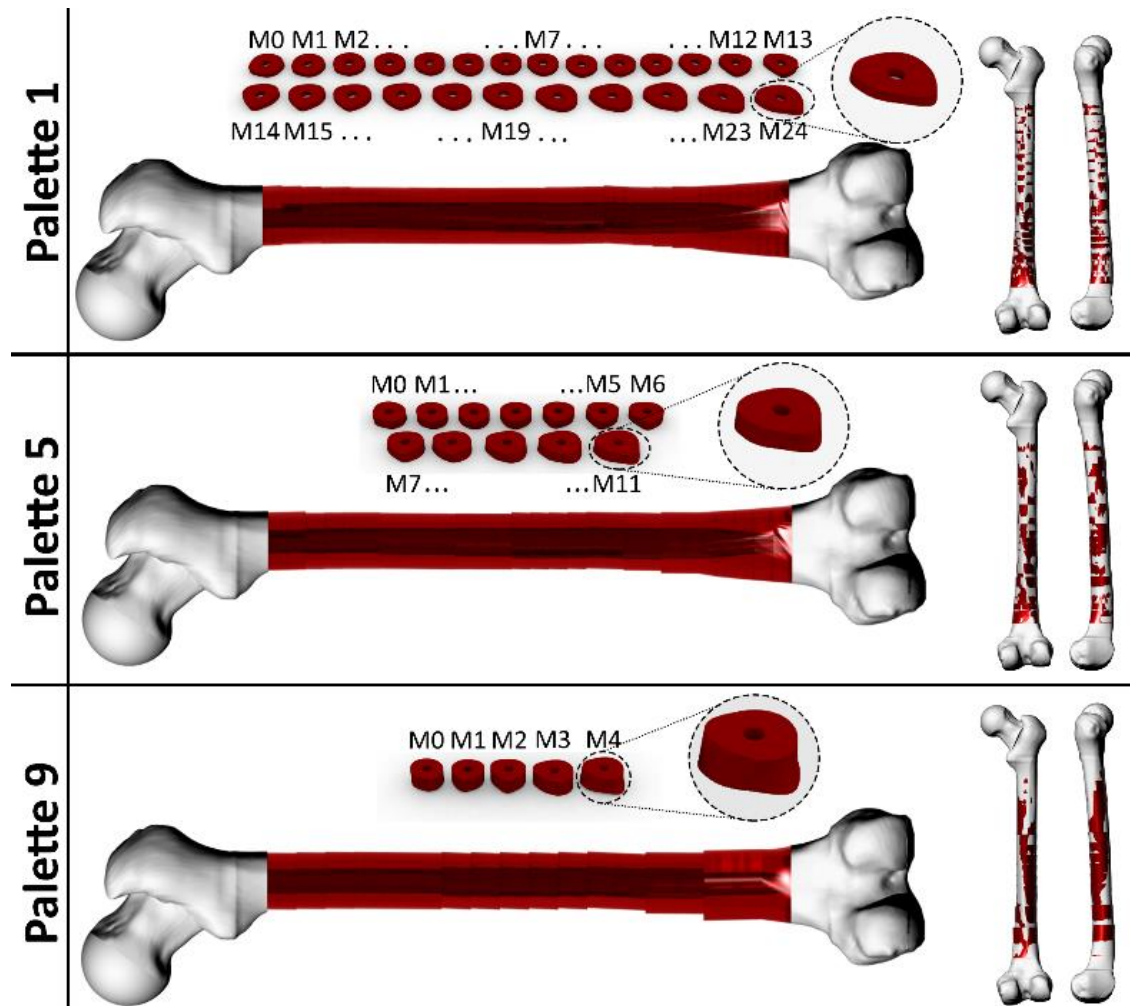
Figure 3.4 Different palettes of scaffold blocks.

In the defined region, due to morphological characteristic of the femur, the topological features of cross-sectional curves regarding the upper part of it are relatively similar to each other. That is why the number of different modules needed to represent this part of the region was less when those of the distal part of the shaft region is considered. So, the majority of the differences in modules occurs in the lower part. Thus, regardless of the module height input, even the tolerance input decreases, the total number of different

modules does not change much after a while. Although the module height input given to the system does not seem to make much change, the effect of module height appears mostly how well the created scaffold structure fits the patient. Another point to consider in the module height decision is that it should also provide enough dimensional flexibility for a surgeon to handle during assembly and implantation.

To illustrate the effect of these parameters on modules and the final scaffold structure, patient specific scaffolds were created with different bone brick palettes for different cases (Figure 3.5). The first scenario was where a large bone defect was observed around the distal part of the shaft region of femur model C. The defect height (the length along sagittal/ coronal plane, Z-axis) was 67.6 mm. The information on where the defect was introduced to the system. The modules belonging to Palette 1,4, and 7, created from femur model B, ware uploaded to the system as default, respectively. As a result, the system gave the best-fitting scaffold to the patient with femur model C (Figure 3.5(e)). Moreover, the information about the assembly of the proper modules was extracted. The same procedure was followed for femur model A with a defect having similar specifications (Figure 3.5(f)). As another scenario, a large bone defect around the middle shaft region was examined for both femur model C and A. The height of this defect was 109.2 mm. After the femur models were generated, the defect area was introduced to the system. Correspondingly, the best fitting scaffold and the assembly information, created with the defined default module palettes, were obtained for both femur models (Figure 3.5(b), (c)).

As it can be seen from the resultant scaffold structures, the scaffolds created with Palette 1 have smoother surfaces than those created with Palette 4 and 7. When the values of the tolerance and height inputs of the Algorithm 2.1 decrease, the representation of the patient femur will be more accurate. Additionally, obtaining a better fitting scaffold structure becomes possible. Nonetheless, one drawback regarding using the Palette 1 is that the total number of different modules is higher, it might be difficult for the surgeon to create a best fitting scaffold for a patient with a large bone defect.

On the other hand, when implanting the created scaffold into the body, the height of the created structure becomes as much important as its accurate surface representation. The clinician needs to make certain changes to the bone tissue in order to clean the defect area from excess, and for the scaffold structure to fit the defect area properly. Performing minimum changes without losing too much of the native tissue is directly related to the

height of the final scaffold structure. The scaffold structure, created with modules belonging to Palette 7 for 67.60 mm sized defect (Figure 3.5(e) and (f)), was the structure where the most changes had to be made due to the height difference between the defect and this scaffold, which was 10.55 mm. It was followed by the scaffold, created with Palette 4 modules, with a height difference of 2.54 mm. However, it was not the same for the scaffolds produced for femur models with 109.20 mm sized shaft defect (Figure 3.5(b) and (c)). Here, the amount of cutting operation needs to be done in the native tissue is more when the scaffold structure was created with modules belonging to Palette 4 rather than Palette 7 (1.02, 0.21 mm respectively). Although the maximum amount of native tissue that needs to be cut has a direct relationship with the module height, it is also affected by the defect height. Therefore, whichever group is targeted, the most common defect in that group can be analyzed by performing a statistical study of the location of the defect and the most common defect height. Based on the results obtained from this analysis, the height of the modules could be decided.

Prototypes of different scaffold structures and femur models were manufactured with commercially available 3D printers and software (Figure 3.5(a) and (d)). Additionally, to be able to produce the scaffolds with the generated novel zig-zag/spiral pattern, scripting tools of Rhinoceros 3D (Rhino Script and Python for Grasshopper) were used to obtain the instruction file to control the custom extrusion based 3D printer. The 3D printer has a heated syringe where 37 kDa molecular weight PCL melted at 65 ^{0}C. With a pneumatic dispensing unit, melted PCL was extruded through a nozzle with 250 μm diameter until the whole modular block was manufactured layer by layer. All the modular blocks used to create the scaffold structure for 67.90 mm distal bone defect were printed (Figure 3.6(a)). Some of them, M3, M6, M9, M12 and different porosity level of M12 can be seen in Figure 3.6 (g), (f), (e), (b), and (c), (d) respectively.

When the same first and second division numbers were used as inputs in the Algorithm 2.2 to produce each module, the location of the pore in each module would be almost the same. Thus, if an obtained scaffold structure, created with such printed modules, is viewed from above, the channels extending all the way through could be seen (Figure 3.6(a)). Using the same parameters also causes the total porosity of the modules to be close to each other (Figure 6(b), (e), (f), (g)).

34

The intramedullary femoral nail will be used to put the modules on top of each other to create the best fitting scaffold structure. Thus, most of the load would be borne by the nail. However, the modular blocks should have adequate mechanical properties for a clinician to handle during the operation. A compression test was performed on the modules shown in Figure 3.6 with a Zwick/Roell Z100 test machine with a 10 kN load cell. The prescribed displacement rate used in the compression test was 0.5 mm/min. The compression tests for each module were performed in the elastic region, and the tests were stopped at the %7 strain. During the test, the force (N) and the deformation (%) were recorded.
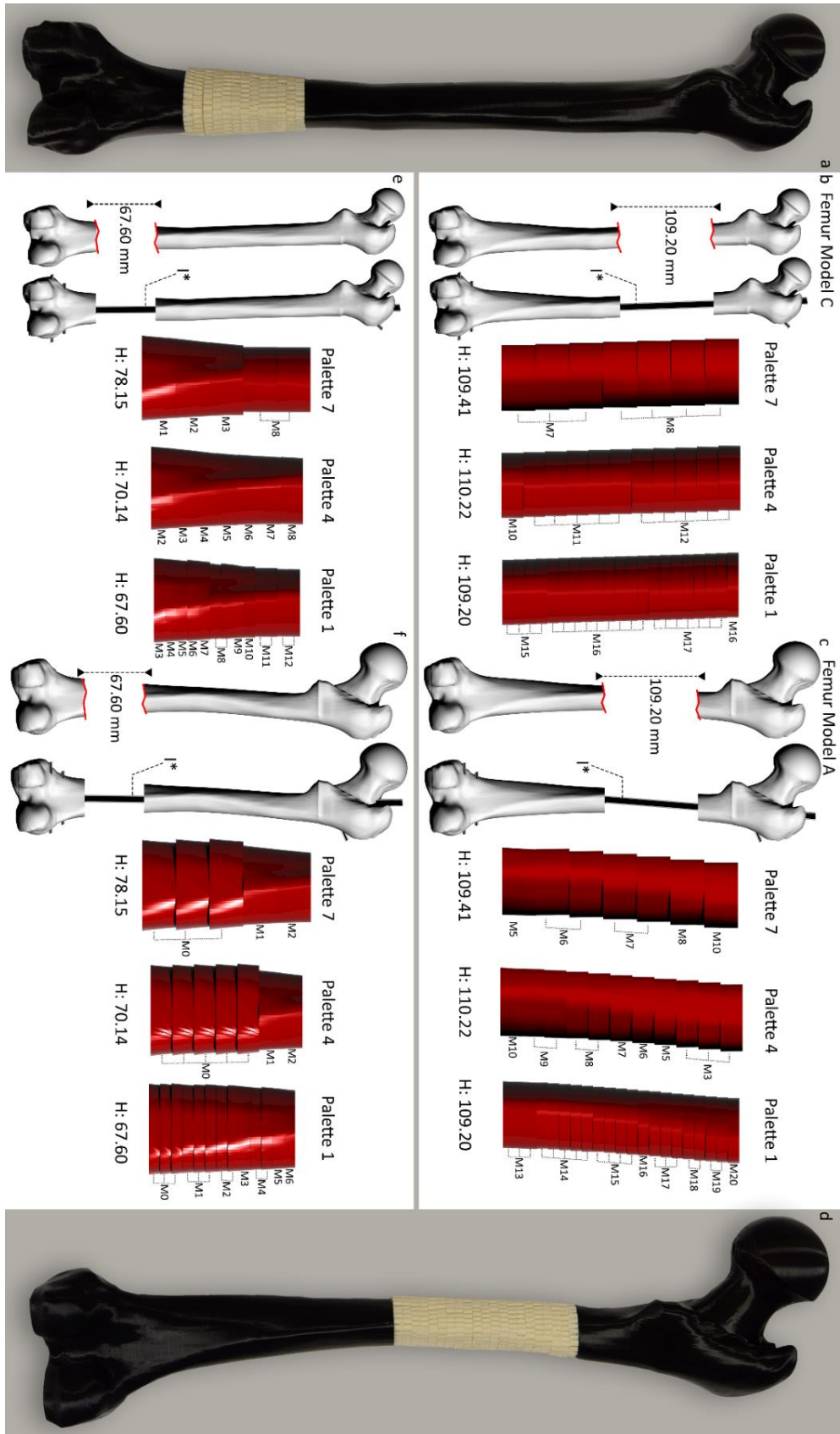
Figure 3.5 Best fitting scaffolds for femur model C (a), (b), (e) and A (c), (d), (f) with 67.60 mm distal (a), (e), (f) and 109.20 mm shaft (b), (c), (d) defect with different palette of bone bricks (Palette 1,4,7). Printed prototypes of femur model C with 67.60.
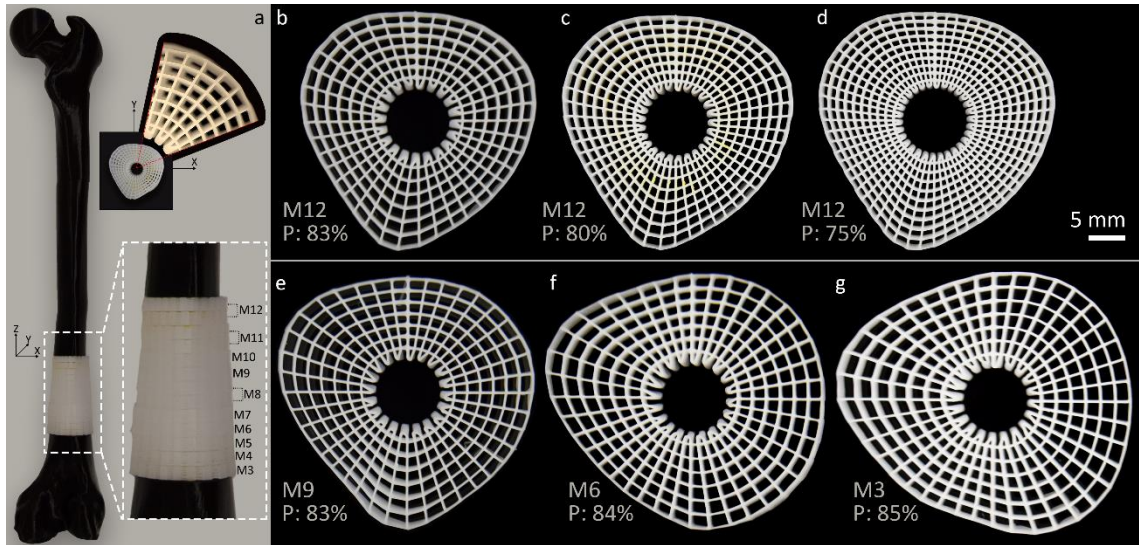
Figure 3.6 (a): The assembly of the best fitting scaffold with modules of Palette 1: M12 (b), M9(e), M6(f), M3(g) which are created with the same inputs of Algorithm 3.2. The top view of created structure. (c), (d): The resultant M12 scaffold blocks with different parameter of Algorithm 3.2.

As it can be seen from Figure 3.7, there is a toe region (Banik, Lewis, and Brown 2016) in the force-strain curves, and it ends around %2 deformation. This could be due to the deflection happened in the deposited strips. Thus, not all the strips were touching the grip of the machine at the same time. Another reason regarding this could be that some of the final printed structures had some wrapping. Due to wrapping, not every part of the blocks starts to touch the grip at the same time as well. Moreover, this toe region could be occurred due to the small forces be applied in the test, or the poor alignment of the grips.

With using the received data (Figure 3.7), and dimensional measurements of the modules, Table 3.4, the equivalent structural stiffness of modules were calculated (Figure 3.8) based on Hook's law and the governing equation of linear elasticity ($\sigma=E\varepsilon$). Based on the results, it could be easily said that the stiffnesses of the structures were appropriate for a clinician to handle.

Table 3.4 Cross-sectional areas of modules in mm^2.

Module	M12_3	M12_2	M12_1	M9	M6	M3
Area	674.17345	674.17345	674.17345	747.78405	874.99933	937.11651
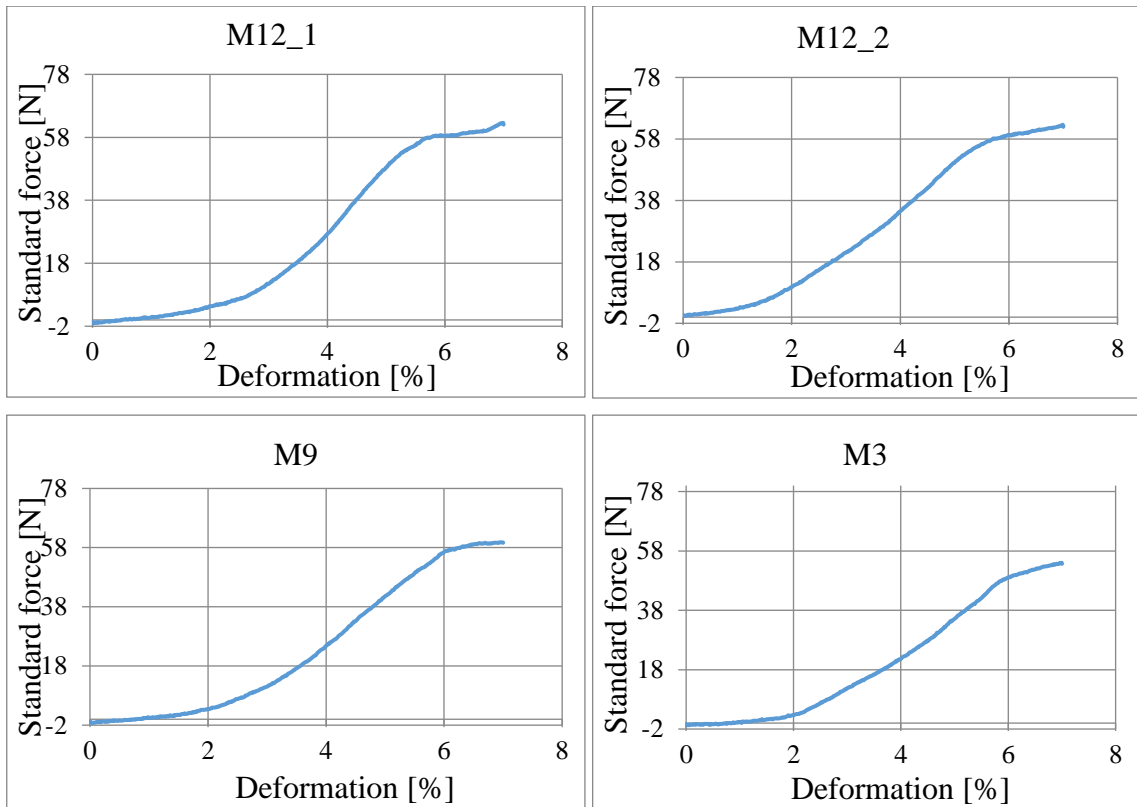
Figure 3.7 Force - deformation graphs of M12_1 (refers to (b) in Figure 2.6), M12_2 (refers to (c) in Figure 2.6), M9 (refers to (e) in Figure 2.6), M3 (refers to (g) in Figure 2.6).

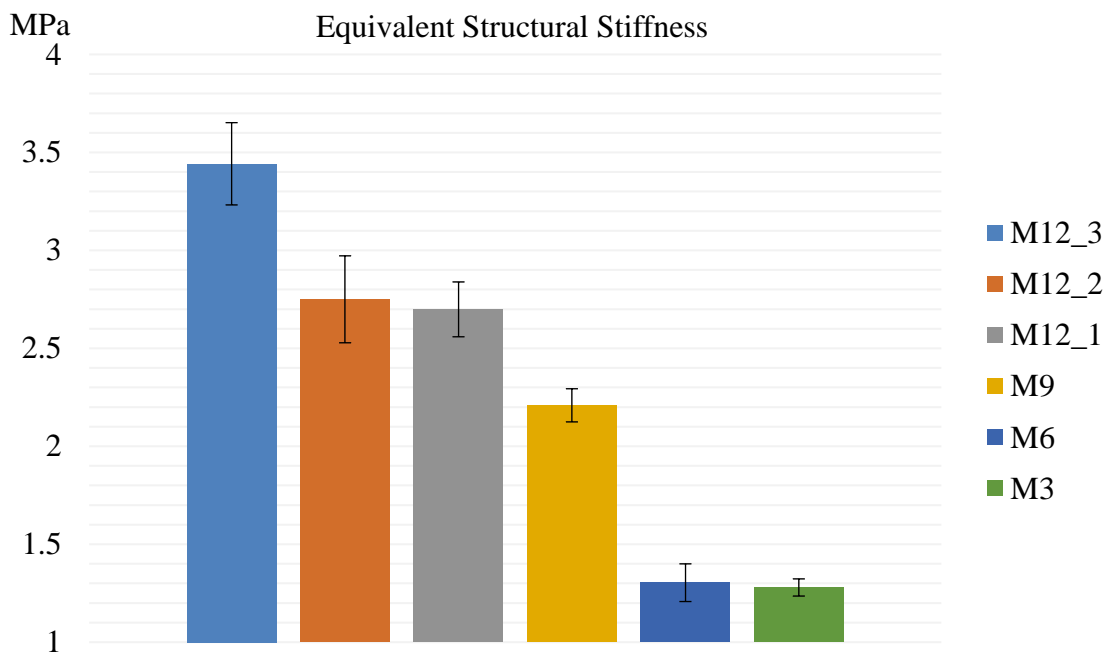Figure 3.8 The equivalent stiffness of modular blocks (M12_3 refers to (d) in Figure 2.6, M12_2 refers to (c) in Figure 2.6, M12_1 refers to (b) in Figure 2.6, M9 refers to (e) in Figure 2.6, M6 refers to (f) in Figure 2.6, M3 refers to (g) in Figure 2.6.

To understand the mechanical properties of the structure (Figure 2.6 (b)), finite element analysis was performed in ANSYS 2020 R1. To create an accurate analysis, it is important to know the mechanical properties of the material used in the printing. In this study, since the module was printed with PCL, to obtain the elastic modulus and yield stress of it, a tensile test of samples, printed with PCL, was performed to obtain the stress-strain curve of printed PCL.
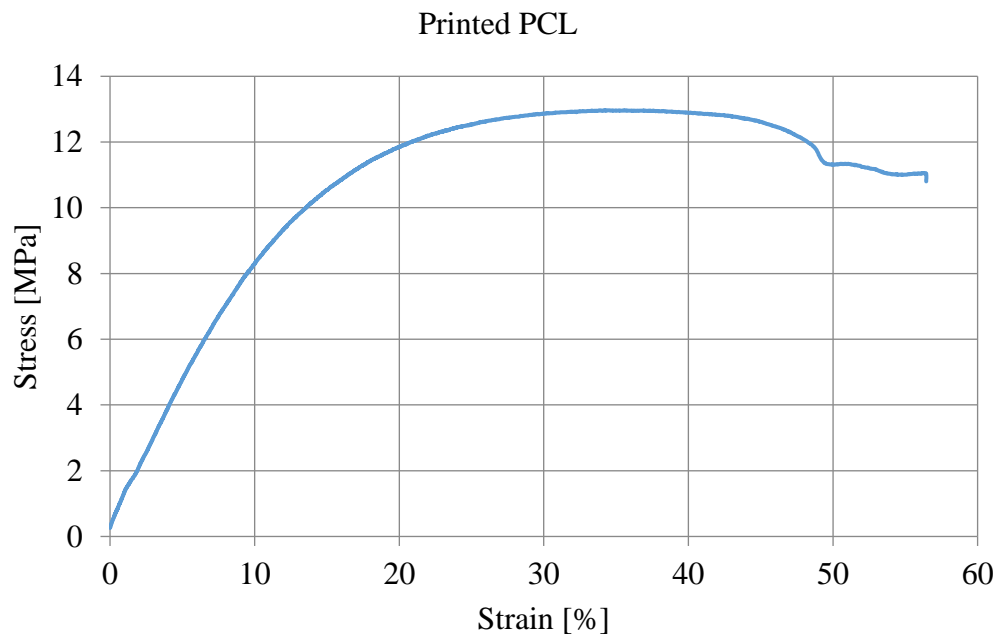
Figure 3.9 - Stress - strain curve of printed PCL.

The extracted elastic modules of the printed PCL from Figure 3.9, which was 85 MPa, was used in the finite element analysis. This value was assigned to the solid part which represents the printed strips. To be able to do a compression test, two cylindrical 3D solid, Figure 3.10, representing the grips of the testing machine, were modeled and assigned a much higher elastic module value than PCL's. The compression test analysis was held with assigning the proper boundary conditions. Fixed support, represented as B in Figure 3.10, was assigned to the bottom plane, while the displacement, represented as A in Figure 3.10, was assigned to the top plane. After meshing completed with linear tetrahedron elements, the analysis was performed. For this structure, the mesh dependency analysis was also done as shown in Figure 3.11. Due to the time and the total number of elements needed in the analysis, 0.3 mm element size was used in the upcoming analysis regarding mesh dependency study. The result of the analysis obtained

based on these setups could be seen in Figure 3.12.

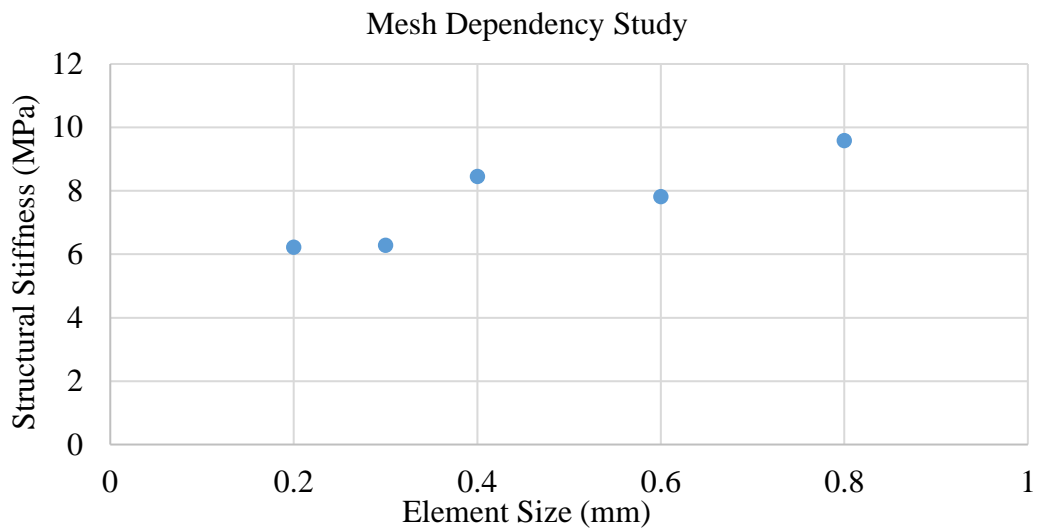Figure 3.10 Set up for finite element analysis.

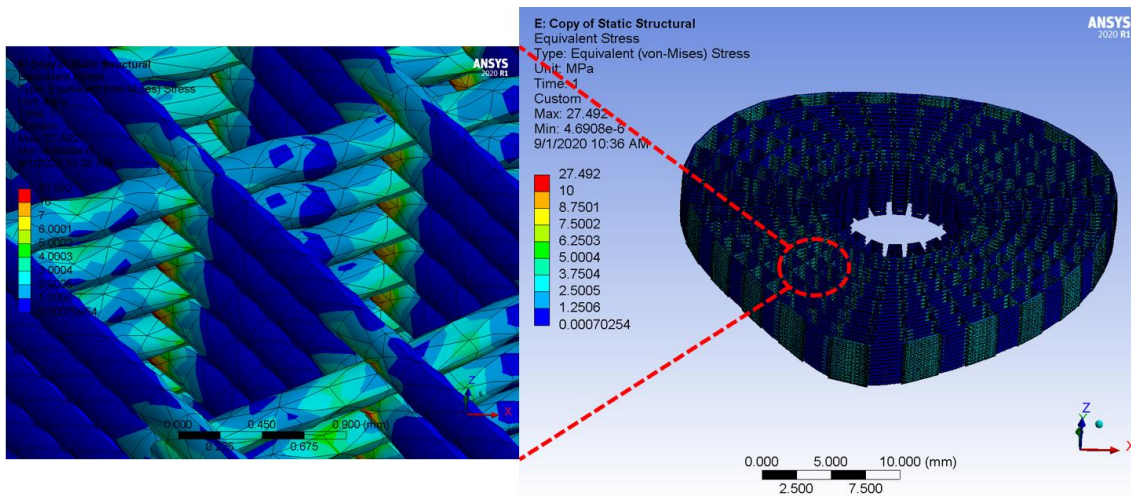Figure 3.11 - Mesh dependency analysis of the structure.

Figure 3.12-Finite element analysis (linear elastic) result of Module 12 in Palette 1.

The other information extracted from Figure 3.9 was the yield stress of printed PCL, which was 8.5 MPa. When the result of the linear elastic analysis is examined, it could be seen that some parts of the structure exceeded the yield stress of the printed PCL. These parts were mostly where the overlaps between layers happen. It means that in these parts, the deformation became plastic rather than elastic. That is why another analysis, linear elastic–plastic, was performed.

To make this analysis, PCL's yield strength, which was 8.5 MPa, and tangent modulus, which was 0.5 MPa, were extracted from printed PCL's stress-strain curve, Figure 3.9. After making the necessary arrangements in the analysis regarding this information, the analysis was performed. The result of this analysis could be seen in Figure 3.13.
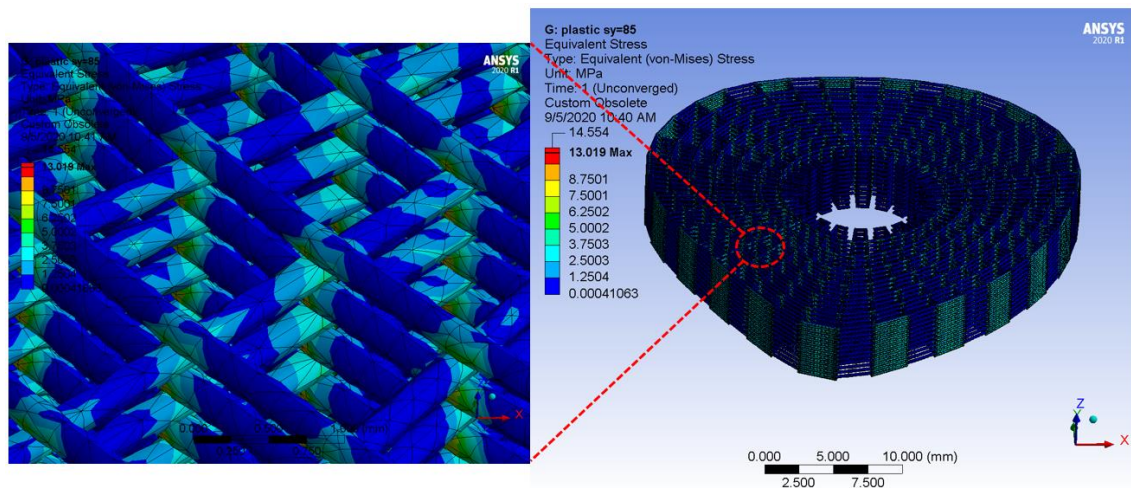
Figure 3.13 - Finite element analysis (linear elastic - plastic) result of Module 12 in Palette 1.

To compare the three obtained results; the experimental, linear elastic analysis, and linear elastic–plastic analysis, a graph was created, Figure 3.14. As could be understood, the equivalent structural stiffness obtained by linear elastic–plastic analysis was much closer to the that of experiment. The structure was formed with strips. For strips to hold on to each other, the overlapping rate between layers is necessary, otherwise printing will not be completed successfully. Thus, plastic deformation due to overlapping was observed.
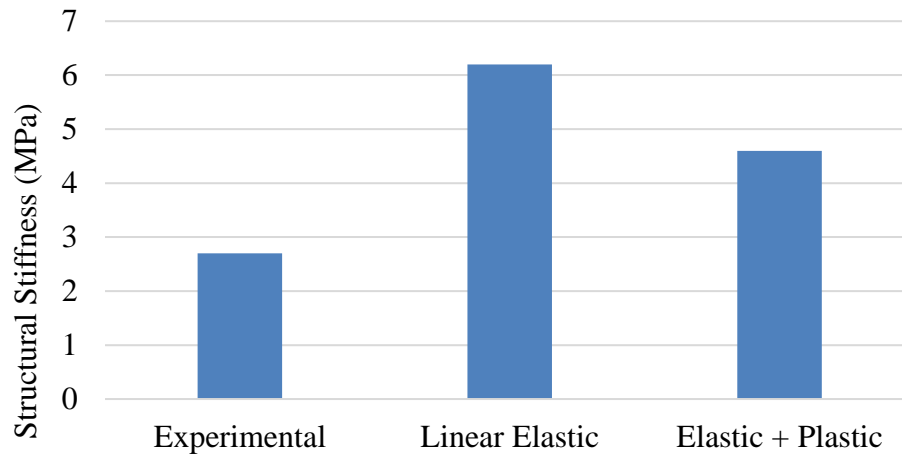
Figure 3.14 - Comparison of the results obtained via; experimental, linear elastic and linear elastic + plastic analysis.

3.8. Conclusion

In this chapter, a new approach to create a customized best fitting scaffold for large bone defects from an already produced modular, bioactive, low-cost bone scaffold blocks was investigated. A femur surface modeling algorithm was developed to generate the femur model of a patient. This algorithm eliminates the most time-consuming, labor-intense, and relatively expensive steps of creating a patient specific scaffolds from (e.g., importing 2D medical images into a medical image processing software for 3D reconstruction of the femur and defect area, and joint work of creating a scaffold between technical and surgical staff). Another algorithm for creating scaffold blocks was generated parametrically so that modules with desired morphological characteristics can be obtained to represent the femur in the best possible way. To mimic the bone morphology and obtain an adequate porous structure, a computational algorithm was generated to create a continuous, zig-zag/spiral tool path for AM of modules. With a custom extrusion-based 3D printer, the porous bone bricks were additively manufactured with a biodegradable polymer. Another algorithm, restoring the information of what the already printed modules are, was created to inform the clinician about how many of which on-demand modules they could use to create a best fitting patient specific scaffold to represent the defect area of that patient. This study represents a promising approach in the creation of a new customized best fitting scaffold with less time, money, and effort for large bone defects.

CHAPTER 4 CONCLUSION AND FUTURE WORK

In Chapter 2, a novel method of biomimetic modeling and additive manufacturing of modular, customizable, porous scaffold blocks has been presented. Computational methods were developed to generate modular blocks where they can be customized for any bone defects by selecting the proper modules and putting them on top of each other. Another algorithm for manufacturing scaffold blocks was generated parametrically so that modules with desired morphological characteristics can be obtained to represent the femur in the best possible way. This computational method generates a continuous deposition path plan where zig-zag pattern and spiral-like pattern follow each other in two consecutive layers continuously, until the 3D porous module is generated. With a custom extrusion-based 3D printer, the designed porous modular blocks were additively manufactured with a biodegradable polymer (PCL) by controlling the porosity and mimicking the actual micro-architecture of the bone. The developed methods can be used to create the best fitting patient-specific scaffolds, using pre-manufactured porous modular blocks to treat critical bone defects.

In Chapter 3, a new approach to create a customized best fitting scaffold for large bone defects from an already produced modular, bioactive, low-cost bone scaffold blocks was investigated. A femur surface modeling algorithm was developed to generate the femur model of a patient. This algorithm eliminates the most time-consuming, labor-intensive, and relatively expensive steps of creating a patient specific scaffold, such as importing 2D medical images into a medical image processing software for 3D reconstruction of the femur and defect area, and joint work of creating a scaffold. Another algorithm, restoring the information of what the already printed modules are, was created to inform the clinician for necessary modules and their sequences so they could use to create a best fitting patient specific scaffold to represent the defect area of that patient. This study represents a promising approach in the creation of a new customized best fitting scaffold

with less time, money, and effort for large bone defects.

As future works;

•   More scaffold with different porosity could be printed, and mechanically and biologically tested to understand the behaviour of the structures. Based on the test results optimum porosity could be obtained. Moreover, with PCL with different combination of different materials (bioceramics, bioactive glasses, polymers) could be used in the manufacturing process and observed the effects of the used material in biomechanical perspectives.

•   In the current design of the modules, there is almost no limitation on rotation around Z-axis while the assembly is being made. The main focuses in this thesis were to create scaffold modules with best fitting external shapes to femur bone and additive manufacture them with a novel toolpath planning for continuous extrusion AM. Since continuous toolpath and extrusion based 3D printing limit the manufacturability, using other types of AM and/or discontinuous toolpath can increase the modification could be made in the design regarding the locking system of the modules during assembly.

BIBLIOGRAPHY

Abd-Khorsand, Saber, Samaneh Saber-Samandari, and Saeed Saber-Samandari. 2017. "Development of Nanocomposite Scaffolds Based on TiO2 Doped in Grafted Chitosan/Hydroxyapatite by Freeze Drying Method and Evaluation of Biocompatibility." *International Journal of Biological Macromolecules* 101 (August): 51–58. https://doi.org/10.1016/j.ijbiomac.2017.03.067.

Arrington, Edward D., William J. Smith, Henry G. Chambers, Allan L. Bucknell, and Nelson A. Davino. 1996. "Complications of Iliac Crest Bone Graft Harvesting." *Clinical Orthopaedics and Related Research*, no. 329: 300–309. https://doi.org/10.1097/00003086-199608000-00037.

Ashman, O., and A. M. Phillips. 2013. "Treatment of Non-Unions with Bone Defects: Which Option and Why?" *Injury* 44 (SUPPL.1). https://doi.org/10.1016/S0020-1383(13)70010-X.

Banwart, J. Christopher, Marc A. Asher, and Ruth S. Hassanein. 1995. "Iliac Crest Bone Graft Harvest Donor Site Morbidity: A Statistical Evaluation." *Spine* 20 (9): 1055–66. https://doi.org/10.1097/00007632-199505000-00012.

Bartolo, Paulo, Jean Pierre Kruth, Jorge Silva, Gideon Levy, Ajay Malshe, Kamlakar Rajurkar, Mamoru Mitsuishi, Joaquim Ciurana, and Ming Leu. 2012. "Biomedical Production of Implants by Additive Electro-Chemical and Physical Processes." *CIRP Annals - Manufacturing Technology* 61 (2): 635–55. https://doi.org/10.1016/j.cirp.2012.05.005.

Bose, Susmita, Sahar Vahabzadeh, and Amit Bandyopadhyay. 2013. "Bone Tissue Engineering Using 3D Printing." *Materials Today*. Elsevier. https://doi.org/10.1016/j.mattod.2013.11.017.

Caetano, Guilherme, Ricardo Violante, Ana Beatriz Sant´Ana, Adriana Batista Murashima, Marco Domingos, Andrew Gibson, Paulo Bártolo, and Marco Andrey Frade. 2016. "Cellularized versus Decellularized Scaffolds for Bone

Regeneration." *Materials Letters* 182 (November): 318–22.
https://doi.org/10.1016/j.matlet.2016.05.152.

Campana, V., G. Milano, E. Pagano, M. Barba, C. Cicione, G. Salonna, W. Lattanzi,
and G. Logroscino. 2014. "Bone Substitutes in Orthopaedic Surgery: From Basic
Science to Clinical Practice." *Journal of Materials Science: Materials in Medicine*
25 (10): 2445–61. https://doi.org/10.1007/s10856-014-5240-2.

Chantarapanich, Nattapon, Sattaya Rojanasthien, Bancha Chernchujit, Banchong
Mahaisavariya, Kavin Karunratanakul, Prasert Chalermkarnnon, Chinnawit
Glunrawd, and Kriskrai Sitthiseripratip. 2017. "3D CAD/Reverse Engineering
Technique for Assessment of Thai Morphology: Proximal Femur and
Acetabulum." *Journal of Orthopaedic Science* 22 (4): 703–9.
https://doi.org/10.1016/j.jos.2017.02.003.

Chen, Xiaozhong, Kunjin He, Zhengming Chen, and Lin Wang. 2016. "A Parametric
Approach to Construct Femur Models and Their Fixation Plates." *Biotechnology &
Biotechnological Equipment* 30 (3): 529–37.
https://doi.org/10.1080/13102818.2016.1145555.

Chen, Xiaozhong, Kunjin He, Zhengming Chen, and Wei Xiang. 2015. "Quick
Construction of Femoral Model Using Surface Feature Parameterization." *MCB*.
Vol. 12.

Costantini, Marco, Cristina Colosi, Pamela Mozetic, Jakub Jaroszewicz, Alessia Tosato,
Alberto Rainer, Marcella Trombetta, Wojciech więszkowski, Mariella Dentini, and
Andrea Barbetta. 2016. "Correlation between Porous Texture and Cell Seeding
Efficiency of Gas Foaming and Microfluidic Foaming Scaffolds." *Materials
Science and Engineering C* 62 (May): 668–77.
https://doi.org/10.1016/j.msec.2016.02.010.

DeCoster, Thomas A., Rick J. Gehlert, Elizabeth A. Mikola, and Miguel A. Pirela-Cruz.
2004. "Management of Posttraumatic Segmental Bone Defects." *The Journal of
the American Academy of Orthopaedic Surgeons*. J Am Acad Orthop Surg.
https://doi.org/10.5435/00124635-200401000-00005.

Denry, Isabelle, and Liisa T. Kuhn. 2016. "Design and Characterization of Calcium

Phosphate Ceramic Scaffolds for Bone Tissue Engineering." In *Dental Materials*, 32:43–53. Elsevier Inc. https://doi.org/10.1016/j.dental.2015.09.008.

Domingos, M., F. Intranuovo, A. Gloria, R. Gristina, L. Ambrosio, P. J. Bártolo, and P. Favia. 2013. "Improved Osteoblast Cell Affinity on Plasma-Modified 3-D Extruded PCL Scaffolds." *Acta Biomaterialia* 9 (4): 5997–6005. https://doi.org/10.1016/j.actbio.2012.12.031.

Ericksen, Mary Frances. 1979. "Aging Changes in the Medullary Cavity of the Proximal Femur in American Blacks and Whites." *American Journal of Physical Anthropology* 51 (4): 563–69. https://doi.org/10.1002/ajpa.1330510408.

Eshraghi, Shaun, and Suman Das. 2010. "Mechanical and Microstructural Properties of Polycaprolactone Scaffolds with One-Dimensional, Two-Dimensional, and Three-Dimensional Orthogonally Oriented Porous Architectures Produced by Selective Laser Sintering." *Acta Biomaterialia* 6 (7): 2467–76. https://doi.org/10.1016/j.actbio.2010.02.002.

Fereshteh, Zeinab, Mohammadhossein Fathi, Akbar Bagri, and Aldo R. Boccaccini. 2016. "Preparation and Characterization of Aligned Porous PCL/Zein Scaffolds as Drug Delivery Systems via Improved Unidirectional Freeze-Drying Method." *Materials Science and Engineering C* 68 (November): 613–22. https://doi.org/10.1016/j.msec.2016.06.009.

Fiedler, T., A. C. Videira, P. Bártolo, M. Strauch, G. E. Murch, and J. M.F. Ferreira. 2015. "On the Mechanical Properties of PLC-Bioactive Glass Scaffolds Fabricated via BioExtrusion." *Materials Science and Engineering C* 57 (August): 288–93. https://doi.org/10.1016/j.msec.2015.07.063.

Flierl, Michael A., Wade R. Smith, Cyril Mauffrey, Kaan Irgit, Allison E. Williams, Erin Ross, Gabrielle Peacher, David J. Hak, and Philip F. Stahel. 2013. "Outcomes and Complication Rates of Different Bone Grafting Modalities in Long Bone Fracture Nonunions: A Retrospective Cohort Study in 182 Patients." *Journal of Orthopaedic Surgery and Research* 8 (1): 33. https://doi.org/10.1186/1749-799X-8-33.

Garg, Tarun, Onkar Singh, Saahil Arora, and R. S.R. Murthy. 2012. "Scaffold: A Novel

Carrier for Cell and Drug Delivery." *Critical Reviews in Therapeutic Drug Carrier Systems*. Begell House Inc. https://doi.org/10.1615/CritRevTherDrugCarrierSyst.v29.i1.10.

Giannoudis, Peter V., Haralambos Dinopoulos, and Eleftherios Tsiridis. 2005. "Bone Substitutes: An Update." *Injury*. https://doi.org/10.1016/j.injury.2005.07.029.

Goulet, R. W., S. A. Goldstein, M. J. Ciarelli, J. L. Kuhn, M. B. Brown, and L. A. Feldkamp. 1994. "The Relationship between the Structural and Orthogonal Compressive Properties of Trabecular Bone." *Journal of Biomechanics* 27 (4): 375–89. https://doi.org/10.1016/0021-9290(94)90014-0.

"Grasshopper." 2020. 2020. http://www.grasshopper3d.com/.

Greenwald, A. S., S. D. Boden, V. M. Goldberg, Y. Khan, C. T. Laurencin, and R. N. Rosier. 2001. "Bone-Graft Substitutes: Facts, Fictions, and Applications." In *Journal of Bone and Joint Surgery - Series A*, 83:98–103. Journal of Bone and Joint Surgery Inc. https://doi.org/10.2106/00004623-200100022-00007.

Ji, Chengdong, Nasim Annabi, Maryam Hosseinkhani, Sobana Sivaloganathan, and Fariba Dehghani. 2012. "Fabrication of Poly-DL-Lactide/Polyethylene Glycol Scaffolds Using the Gas Foaming Technique." *Acta Biomaterialia* 8 (2): 570–78. https://doi.org/10.1016/j.actbio.2011.09.028.

Keating, John F., A. H.R.W. Simpson, and C. M. Robinson. 2005. "The Management of Fractures with Bone Loss." *Journal of Bone and Joint Surgery - Series B*. The British Editorial Society of Bone and Joint Surgery. https://doi.org/10.1302/0301-620X.87B2.15874.

Kerley, Ellis R. 1978. "Forensic Anthropology: The Structure, Morphology, and Variation of Human Bone and Dentition. By Mahmoud Y. El-Najjar and K. Richard McWilliams. Charles C Thomas, Springfield, Illinois 1978. Xiv–190 Pp., Tables, Figures, Bibliography, Index. $12.50 (Cloth)." *American Journal of Physical Anthropology* 49 (3): 395–96. https://doi.org/10.1002/ajpa.1330490316.

Khoda, A. K.M., Ibrahim T. Ozbolat, and Bahattin Koc. 2013. "Designing Heterogeneous Porous Tissue Scaffolds for Additive Manufacturing Processes."

CAD Computer Aided Design 45 (12): 1507–23.
https://doi.org/10.1016/j.cad.2013.07.003.

Khoda, A. K.M.Bashirul, and Bahattin Koc. 2013. "Functionally Heterogeneous Porous
Scaffold Design for Tissue Engineering." *CAD Computer Aided Design* 45 (11):
1276–93. https://doi.org/10.1016/j.cad.2013.05.005.

Kim, Tiffany, Carmine Wang See, Xiaochun Li, and Donghui Zhu. 2020. "Orthopedic
Implants and Devices for Bone Fractures and Defects: Past, Present and
Perspective." *Engineered Regeneration* 1 (January): 6–18.
https://doi.org/10.1016/j.engreg.2020.05.003.

Koc, B., A.A. Acar, A. Weightman, G. Cooper, G. Blunn, and P. Bartolo. 2019.
"Biomanufacturing of Customized Modular Scaffolds for Critical Bone Defects."
CIRP Annals 68 (1). https://doi.org/10.1016/j.cirp.2019.04.106.

Li, Guoyuan, Lei Wang, Wei Pan, Fei Yang, Wenbo Jiang, Xianbo Wu, Xiangdong
Kong, Kerong Dai, and Yongqiang Hao. 2016. "In Vitro and in Vivo Study of
Additive Manufactured Porous Ti6Al4V Scaffolds for Repairing Bone Defects."
Scientific Reports 6 (1): 1–11. https://doi.org/10.1038/srep34072.

Liu, Xiaohua, and Peter X. Ma. 2004. "Polymeric Scaffolds for Bone Tissue
Engineering." *Annals of Biomedical Engineering* 32 (3): 477–86.
https://doi.org/10.1023/B:ABME.0000017544.36001.8e.

Mahaisavariya, Banchong, Kriskrai Sitthiseripratip, Trongtum Tongdee, Erik L.J.
Bohez, Jos Vander Sloten, and Philip Oris. 2002. "Morphological Study of the
Proximal Femur: A New Method of Geometrical Assessment Using 3-Dimensional
Reverse Engineering." *Medical Engineering and Physics* 24 (9): 617–22.
https://doi.org/10.1016/S1350-4533(02)00113-3.

Masquelet, A C, F Fitoussi, T Begue, and G P Muller. 2000. "Reconstruction of the
long bones by the induced membrane and spongy autograft." *Annales de chirurgie
plastique et esthetique* 45 (3): 346–53.

McCall, Todd A., David S. Brokaw, Bradley A. Jelen, D. Kevin Scheid, Angela V.
Scharfenberger, Dean C. Maar, James M. Green, et al. 2010. "Treatment of Large

Segmental Bone Defects with Reamer-Irrigator-Aspirator Bone Graft: Technique and Case Series." *Orthopedic Clinics of North America*. Orthop Clin North Am. https://doi.org/10.1016/j.ocl.2009.08.002.

Moghadam, M. Zahedi, Sh Hassanajili, F. Esmaeilzadeh, M. Ayatollahi, and M. Ahmadi. 2017. "Formation of Porous HPCL/LPCL/HA Scaffolds with Supercritical CO2 Gas Foaming Method." *Journal of the Mechanical Behavior of Biomedical Materials* 69 (May): 115–27. https://doi.org/10.1016/j.jmbbm.2016.12.014.

Nandakumar, Anandkumar, Hugo Fernandes, Jan de Boer, Lorenzo Moroni, Pamela Habibovic, and Clemens A. van Blitterswijk. 2010. "Fabrication of Bioactive Composite Scaffolds by Electrospinning for Bone Regeneration." *Macromolecular Bioscience* 10 (11): 1365–73. https://doi.org/10.1002/mabi.201000145.

Noble, P. C., J. W. Alexander, L. J. Lindahl, D. T. Yew, W. M. Granberry, and H. S. Tullos. 1988. "The Anatomic Basis of Femoral Component Design." *Clinical Orthopaedics and Related Research*, no. 235 (October): 148–65. https://doi.org/10.1097/00003086-198810000-00015.

Papakostidis, C., M. Bhandari, and P. V. Giannoudis. 2013. "Distraction Osteogenesis in the Treatment of Long Bone Defects of the Lower Limbs: Effectiveness, Complications and Clinical Results; a Systematic Review and Meta-Analysis." *Bone and Joint Journal*. British Editorial Society of Bone and Joint Surgery. https://doi.org/10.1302/0301-620X.95B12.32385.

Pereira, Rúben F., and Paulo J. Bártolo. 2015. "3D Bioprinting of Photocrosslinkable Hydrogel Constructs." *Journal of Applied Polymer Science*. John Wiley and Sons Inc. https://doi.org/10.1002/app.42458.

Perry, Clayton R. 1999. "Bone Repair Techniques, Bone Graft, and Bone Graft Substitutes." In *Clinical Orthopaedics and Related Research*, 71–86. Lippincott Williams and Wilkins. https://doi.org/10.1097/00003086-199903000-00010.

Pirhonen, E., L. Moimas, and J. Haapanen. 2003. "Porous Bioactive 3-D Glass Fiber Scaffolds for Tissue Engineering Applications Manufactured by Sintering Technique." In *Key Engineering Materials*, 240–242:237–40. Trans Tech

Publications Ltd. https://doi.org/10.4028/www.scientific.net/kem.240-242.237.

Polo-Corrales, Liliana, Magda Latorre-Esteves, and Jaime E. Ramirez-Vick. 2014. "Scaffold Design for Bone Regeneration." *Journal of Nanoscience and Nanotechnology*. https://doi.org/10.1166/jnn.2014.9127.

Rawal, B. R., Rahul Ribeiro, Rajesh Malhotra, and Naresh Bhatnagar. 2012. "Anthropometric Measurements to Design Best-Fit Femoral Stem for the Indian Population." *Indian Journal of Orthopaedics* 46 (1): 46–53. https://doi.org/10.4103/0019-5413.91634.

"Rhinoceros 3D." 2020. 2020. http://www.rhino3d.com/.

Ros-Tárraga, Patricia, Angel Murciano, Patricia Mazón, Sergio A. Gehrke, and Piedad N. De Aza. 2017. "New 3D Stratified Si-Ca-P Porous Scaffolds Obtained by Sol-Gel and Polymer Replica Method: Microstructural, Mineralogical and Chemical Characterization." *Ceramics International* 43 (8): 6548–53. https://doi.org/10.1016/j.ceramint.2017.02.081.

Schemitsch, Emil H. 2017. "Size Matters: Defining Critical in Bone Defect Size!" *Journal of Orthopaedic Trauma* 31 (10): S20–22. https://doi.org/10.1097/BOT.0000000000000978.

Scholz, Armin O., Sebastian Gehrmann, Martin Glombitza, Robert A. Kaufmann, R. Bostelmann, Sascha Flohe, and Joachim Windolf. 2015. "Reconstruction of Septic Diaphyseal Bone Defects with the Induced Membrane Technique." *Injury* 46 (October): S121–24. https://doi.org/10.1016/S0020-1383(15)30030-9.

Stojkovic, Milos, Jelena Milovanovic, Nikola Vitkovic, Miroslav Trajanovic, Stojanka Arsic, and Milorad Mitkovic. 2012. "Analysis of Femoral Trochanters Morphology Based on Geometrical Model." *Journal of Scientific & Industrial Research*. Vol. 71.

Theodorou, Georgios S., Eleana Kontonasaki, Anna Theocharidou, Athina Bakopoulou, Maria Bousnaki, Christina Hadjichristou, Eleni Papachristou, et al. 2016. "Sol-Gel Derived Mg-Based Ceramic Scaffolds Doped with Zinc or Copper Ions: Preliminary Results on Their Synthesis, Characterization, and Biocompatibility."

International Journal of Biomaterials 2016. https://doi.org/10.1155/2016/3858301.

Turnbull, Gareth, Jon Clarke, Frédéric Picard, Philip Riches, Luanluan Jia, Fengxuan Han, Bin Li, and Wenmiao Shu. 2018. "3D Bioactive Composite Scaffolds for Bone Tissue Engineering." *Bioactive Materials*. KeAi Communications Co. https://doi.org/10.1016/j.bioactmat.2017.10.001.

Vorys, George C., Hanying Bai, Chandhanarat Chandhanayingyong, Chang H. Lee, Jocelyn T. Compton, Jon Michael Caldwell, Thomas R. Gardner, Jeremy J. Mao, and Francis Y. Lee. 2015. "Optimal Internal Fixation of Anatomically Shaped Synthetic Bone Grafts for Massive Segmental Defects of Long Bones." *Clinical Biomechanics* 30 (10): 1114–18. https://doi.org/10.1016/j.clinbiomech.2015.08.016.

Wang, Weiguang, Guilherme Caetano, William Stephen Ambler, Jonny James Blaker, Marco Andrey Frade, Parthasarathi Mandal, Carl Diver, and Paulo Bártolo. 2016. "Enhancing the Hydrophilicity and Cell Attachment of 3D Printed PCL/Graphene Scaffolds for Bone Tissue Engineering." *Materials* 9 (12). https://doi.org/10.3390/ma9120992.

Wu, Ge, Frans C.T. Van Der Helm, H. E.J. Veeger, Mohsen Makhsous, Peter Van Roy, Carolyn Anglin, Jochem Nagels, et al. 2005. "ISB Recommendation on Definitions of Joint Coordinate Systems of Various Joints for the Reporting of Human Joint Motion - Part II: Shoulder, Elbow, Wrist and Hand." *Journal of Biomechanics* 38 (5): 981–92. https://doi.org/10.1016/j.jbiomech.2004.05.042.

Wu, X., Y. Liu, X. Li, P. Wen, Y. Zhang, Y. Long, X. Wang, Y. Guo, F. Xing, and J. Gao. 2010. "Preparation of Aligned Porous Gelatin Scaffolds by Unidirectional Freeze-Drying Method." *Acta Biomaterialia* 6 (3): 1167–77. https://doi.org/10.1016/j.actbio.2009.08.041.

Yang, Youwen, Guoyong Wang, Huixin Liang, Chengde Gao, Shuping Peng, Lida Shen, and Cijun Shuai. 2019. "Additive Manufacturing of Bone Scaffolds." *International Journal of Bioprinting*. Whioce Publishing Pte. Ltd. https://doi.org/10.18063/IJB.v5i1.148.

Zadpoor, Amir A. 2020. "Meta-Biomaterials." *Biomaterials Science* 8 (1): 18–38.

https://doi.org/10.1039/c9bm01247h.

Zhang, Lei, Guojing Yang, Blake N. Johnson, and Xiaofeng Jia. 2019. "Three-
Dimensional (3D) Printed Scaffold and Material Selection for Bone Repair." *Acta
Biomaterialia*. Acta Materialia Inc. https://doi.org/10.1016/j.actbio.2018.11.039.